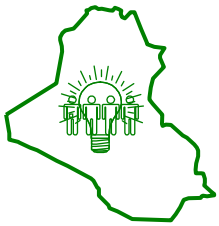

SPONSORED AND PUBLISHED BY
THE IRAQI SOCIETY FOR ALTERNATIVE AND RENEWABLE ENERGY SOURCES AND TECHNIQUES (I.S.A.R.E.S.T.)

EDITORIAL BOARD

ADVISORY BOARD

Recent Developments in p-type and n-type TCOs and Their applications

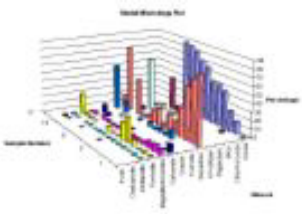

Written by
Raid A. Ismail (*professor*)
University of Hadhramout, Yemen

One of the most important fields of interest in materials science is the fundamental aspects and applications of semiconducting transparent films, which are known as "Transparent Conducting Oxides" (TCOs) in opto-electronic devices technologies. These fascinating films have high electrical conductivity ($\geq 10^3 S.cm^{-1}$) at 300K and high average optical transparency (>80%) in the visible region. TCOs are well known and widely used for a long time in optoelectronic industries as well as in research fields. After the first report of transparent conducting cadmium oxide (CdO) thin films by Badekar in 1907, extensive works had been carried out in the field of TCO technology to prepare new types of TCOs with wide ranging applications. Some of these well known and widely used TCOs include In_2O_3:Sn/F/Sb/Pb, ZnO:In/Al/F/B/Ga, Cd_2SnO_4, SnO_2: Sb/F *etc*. as well as some new TCOs such as $CdIn_2O_4$:Sn, $CdSb_2O_6$:Y, $GaInO_3$:Ge/Sn, $AgInO_2$:Sn, $MgIn_2O_4$,$In_4Sn_3O_{12}$, Zn_2SnO_4, etc.

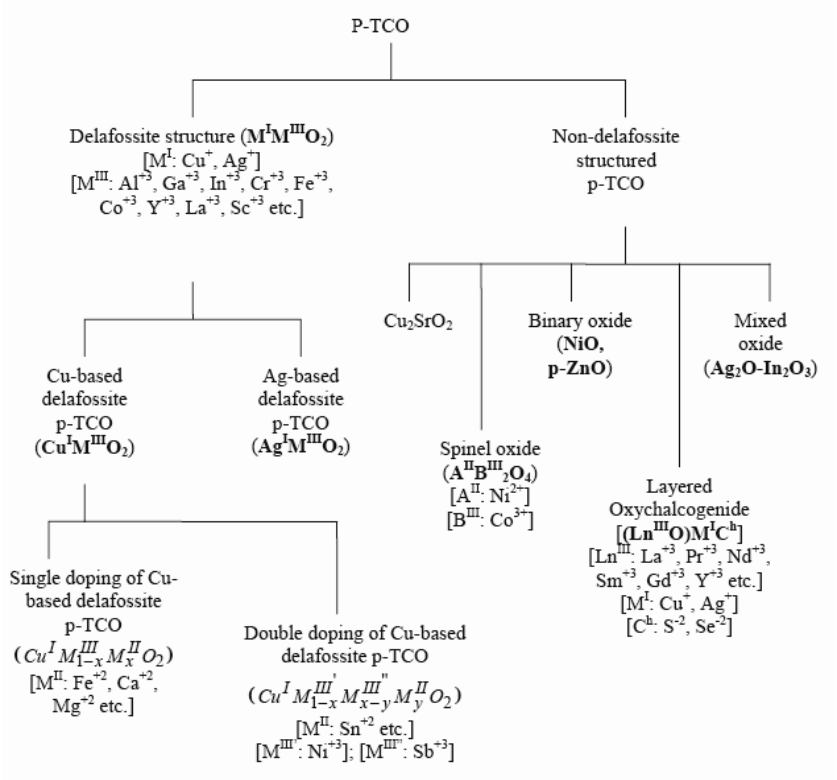

A TCO is a wide band-gap semiconductor that has a relatively high concentration of free electrons in its conduction band. These arise either from defects in the material or from extrinsic dopants, the impurity levels of which lie near the conduction band edge. The high-electron-carrier concentration (the materials will be assumed to be n-type unless otherwise specified) causes absorption of electromagnetic radiation in both the visible and infrared portions of the spectrum. For the present purposes, it is the former that is the more important. Because a TCO must necessarily represent a compromise between electrical conductivity and optical transmittance, a careful balance between the properties is required. Reduction of the resistivity involves either an increase in the carrier concentration or in the mobility. Increasing the former also leads

to an increase in the visible absorption. Increasing the mobility, however, has no deleterious effect and is probably the best direction to follow. Achieving high-carrier mobility will necessarily improve the optical properties.

These TCOs are being used extensively in various fields, which include solar cells, photovoltaic devices, heterojunction photodetectors, flat panel displays (FPD), low-emissivity ("low-e") windows, electromagnetic shielding of cathode-ray tubes in video display terminals, electrochromic (EC) materials in rear-view mirrors of automobiles, EC-windows for privacy (so-called "smart windows"), oven windows, touch-sensitive control panels, defrosting windows in refrigerators and airplanes, invisible security circuits, gas sensors, biosensors, corrosion resistant coatings, abrasion resistant coatings , organic light emitting diodes(OLED), polymer light emitting diodes (PLED), antistatic coatings on instruments panels, cold heat mirrors, Ohmic contact for LED, etc. Also some new applications of TCOs have been proposed recently as holographic recording medium, high-refractive index waveguide overlays for sensors and telecommunication applications and write-once read-many-times memory chips (WORM).

Possibility of the above-mentioned novel applications of TCOs is based on the fact that the electronic band gap of a TCO is higher than 3.1eV (corresponding to the energy of a 400 nm blue photon). So visible photons (having energy between 2.1eV to 3.1eV) cannot excite electrons from valence band (VB) to the conduction band (CB) and hence are transmitted through it, whereas they have enough energy to excite electrons from donor level to CB (for n-type TCO) or holes from acceptor level to VB (for p-type TCO). These acceptor donor levels are created in the TCOs by introducing non-stoichiometery and (or) appropriate. Although the TCOs have vast range of applications as mentioned above, very little work have been done on the active device fabrication using TCOs. This is because most of the aforementioned TCOs are n-type semiconductors. The corresponding p-type transparent conducting oxide (p-TCO), which are essential for photovoltaic devices, were surprisingly missing in thin film form for a long time until in 1997, Kawazoe and co-authors reported the p-type conductivity in a highly transparent thin film of copper aluminum oxide($CuAlO_{2+x}$). This has opened up a new field in optoelectronics device technology, the so-called "Transparent Electronics" or "Invisible Electronics", where a combination of the two types of TCOs in the form of a p-n junction could lead to a 'functional' window which transmits visible portion of solar radiation, yet generates electricity by the absorption of UV part. It must be mentioned here that the first report of semi-transparent p-type conducting thin film of nickel oxide was published in 1993 by Sato et al. They observed only 40% transmittance of the NiO films in the visible region and when they tried to fabricate an all-TCO p-i-n diode of the form p-NiO/i-NiO/i-ZnO/n-ZnO, the visible transmittance further reduced to almost 20%. Although this low transmittance was not favorable for superior device applications, but still this report was an important milestone in the field of "Transparent Electronics" and in the development of TCO technology. Copper aluminum oxide ($CuAlO_2$) is the first and the most important p-TCO material reported in thin film form, which has reasonable optical and electrical properties for diverse device applications. The reported visible transparency of this material is around 80% with a direct band gap value of 3.5eV. Figure (1) gives some common p-TCOs materials.

For future optoelectronic device applications, next generation TCO materials must be far more conductive, while preserving or improving transparency and maintaining an appreciable band gap (for optical transparency). The most attractive way to achieve these ends is by increasing carrier mobility since this has no detrimental effects on optical properties. An optimum carrier concentration that maximizes the band gap via the carrier concentration-sensitive Moss- Burstein shift yet maintains a plasma edge removed from the visible region, is desired and in principle achievable via aliovalent doping and/or careful control of the film growth process parameters. Variety techniques were used to prepare TCOs films such as thermal evaporation, pulsed laser depositions (PLD), spray pyrolysis, metal organic chemical vapor deposition (MOCVD), rapid photo-thermal oxidation (RPO), chemical bath deposition (CBD), sputtering, etc.

References

1- Kawazoe, H.; Yasukawa, M.; Hyodo, H.; Kurita, M.; Yanagi, H.; Hosono, H, *Nature* 1997, 389, 939.

2- Yanagi, H.; Inoue, S.; Ueda, K.; Kawazoe, H.; Hosono, H.; Hamada, N, *J. Appl. Phys.* 2000, 88, 4159.

3- Arghya N. Banerjee and Kalyan K. Chattopadhyay, Materials Science Research Trends, ISBN: 978-1-60021-654-1, 2007 Nova.

4- S. Jin, Y. Yang, J. Medvedeva, J. Ireland, A. Metz, *J. Am. Chem. Soc.* 2004, 126, 137, 87.

5- R. A. Ismail, O. A. Abdulrazaq; *Solar Energy Materials & Solar cells* 2007, 9, 903.

Organized by I.S.A.R.E.S.T.

INVITATION TO PARTICIPATE

WHAT IS ENERGY?

Energy is neither created nor destroyed. This is called the principle of Conservation of Energy. In other words, the amount of energy in the universe always remains the same. And when we use energy, like burning wood to generate light and heat, we don't use it up; we simply transform it from one form of potential energy (fuel) into other forms of kinetic energy (heat and light).

Almost all energy transformations involve the production of heat, which is considered the lowest form of energy, because it quickly dissipates into the surroundings and is normally unavailable for further use. So, although the total amount of energy remains the same, the amount of "useable" energy constantly decreases. However, don't worry too much about the decrease of useable energy; our Sun is scheduled to produce solar energy for many years to come, so taking this course will not be a waste of your time (or energy).

Energy is all around us. It heats our homes, powers our light bulbs and appliances, fuels our cars and provides for a variety of professional careers that deal with its many elements. It also comes in many forms such as heat, light, chemical, mechanical and electrical energy. And, according to physicists, energy can neither be created nor destroyed, only converted from one form to another. So why learn about energy? The answer is because energy, and the conversion of energy from one form to another, is fundamental to our modern living environment. By knowing the principles behind energy generation and conversion, you will come away with a knowledge base that can be applied to nearly every modern electrical, mechanical and chemical device that uses or produces power.

To introduce more about the alternative and renewable energy sources and techniques, I.S.A.R.E.S.T. invites you to attend the scientific lectures organized by I.S.A.R.E.S.T. You are requested to contact the secretary of the society and register your attendance. The lectures can be held earlier due to the registered requests.

To all they would like to submit seminars or scientific lectures during the third semester of the **I.S.A.R.E.S.T.** (July, August and September) in 2008, you are kindly requested to contact the secretary of the **I.S.A.R.E.S.T.** for date and presentation arrangements of the seminars or lectures. Please, do not hesitate to participate in our activities, this chance might be required by young scientists in our country, IRAQ, to develop and grow as well as introduce the professors and experts in field. You could find us on the post address, emails and mobile below:

Mailing Address:

P. O. Box 55259, Baghdad 12001, IRAQ

Emails:

irq_appl_phys@yahoo.com

editor_ijap@yahoo.co.uk

odayata2001@yahoo.com

Mobile:

00964-7901274190

Iraqi J. of Appl. Phys. , Vol. 4 , No. 1 , 2008 , 5-9

Determination of Electron Temperatures in Rare-Gases Plasma

Faez M. Ibraheem

Department of Physics,
College of Science,
University of Al-Fateh,
Tripoli, Libya
faez_ibraheem@hotmail.com

Trace rare gases optical emission spectroscopy has been used to measure the electron temperature (T_e) in a high-density inductively coupled dichloride-argon (Cl_2-Ar) plasma at 0.018Torr as function of the radio-frequency power of 13.56MHz frequency and argon (Ar) fraction. Only the krypton (Kr) and xenon (Xe) emission lines were used to determine electron temperature (T_e) because of evidence of radiation trapping, when the argon emission lines were also used for larger Ar fractions. At 600W, electron temperature (T_e) increases from 4.06±0.5eV to 6.06±2.0eV as the Ar fraction increases from 1% to 96%. In the inductive mode, electron temperature (T_e) for chlorine plasma, including 1% of each He, Ne, Ar, Kr and Xe, increases only slightly from 3.8eV to 4.0eV as power increases from 450W to 750W. This increase is much larger for larger Ar fractions, such as from 4.0eV to 7.3eV for 78% Ar. Most of these effects can be understood using the fundamental particle balance equation.

Keywords: *Discharge Plasma, Rare-Gases Plasma, Electron Temperature, Inductively-Coupled Plasma*
Received 4 January 2004, Revised 4 March 2005, Accepted 25 March 2008

1. Introduction

Chlorine-argon plasmas are being investigated for the etching of Si and various III–V materials [1–7]. Previously measurements of the absolute densities of Cl_2, Cl, Cl_2^+, Cl^+, and Ar^+ in inductively coupled plasma (ICP) containing such mixtures were reported. Such measurements should be useful to investigations of the etch mechanism, rate, selectivity, and etched profile shapes [1]. Accurate determination of the electron temperature (T_e) is important for determining the rates of dissociation of Cl_2 and ionization of Cl_2, Cl, and Ar, and in assessing the mechanisms for differential charging. The electron energy distribution function (EEDF) (and therefore T_e) can affect the undesirable etched profile anomalies, such as bowing and microtrenching, and electrical damage due to charge build-up and current flow, as have been observed in the etching of silicon device materials (e.g., Si and Al) [8-10].

Eddy et al. have used a Langmuir probe to measure T_e as a function of radio-frequency (RF) power and Ar fraction in Cl_2–Ar electron cyclotron resonance discharges [2]. However, it is known that such probes are sensitive to the intermediate energy range of the EEDF and there may be a non-Maxwellian high-energy tail [11,12] in these argon-containing discharges (mTorr pressure regime) to which these probes may be relatively insensitive.

To this end, this paper reports measurements of T_e versus RF power and Ar fraction in an ICP Cl_2–Ar discharge using **T**race **R**are **G**ases **O**ptical **E**mission **S**pectroscopy (TRG-OES), a technique sensitive to the high-energy tail (electron energies >9.8eV) of the EEDF [13].

2. Experiment

The ICP reactor, collection and detection optics, and data acquisition system used in these experiments have been described previously [1,14]. A 5% (1.2 SCCM) trace rare gas equimixture of He, Ne, Ar, Kr and Xe was added to the Cl_2–Ar gas mixture for T_e measurements at 0.018Torr. The pressure was the same with the plasma on or off. It is not surprising that the pressure in these Cl_2–Ar discharges is the same for the plasma on and off, since the mean free path for neutrals (~0.3cm) is much less than the diameter (~10.7cm) of the adjoining tube between the reactor and the pumping system [15–16]. Each rare gas fraction differs marginally from the expected 1% value owing to the relative pumping speeds and transport efficiencies of each gas. These effects are taken into account [13] in determining T_e. A 5cm-diameter Si <100> wafer (2–5Ω.cm, n-type, P-doped) covered with a 100nm thick layer of SiO_2 was soldered to the sample holder using indium foil. Silicon dioxide etching in Cl_2 discharges proceeds very slowly, and without bias delivered to the sample holder etching occurs at a rate <0.5nm/min, so the plasma remains relatively unperturbed by any etch products. All measurements are made in the ICP inductive

mode (13.56 MHz RF power >330W for Cl_2 plasmas).

The line-integrated plasma induced emission from a region across the wafer and ~1.5cm above it was collected through one of the UV grade quartz windows of the reactor and focused onto the entrance slit of the monochromator. It was scanned from 745nm to 885nm (for various Ar, Kr, and Xe emission lines employed in the TRG-OES model) at rates varying from 0.2nm/s to 0.5nm/s with a 0.175nm bandpass to acquire the necessary emission lines. The emission intensities were corrected for the relative spectral dependencies of the monochromator and photomultiplier.

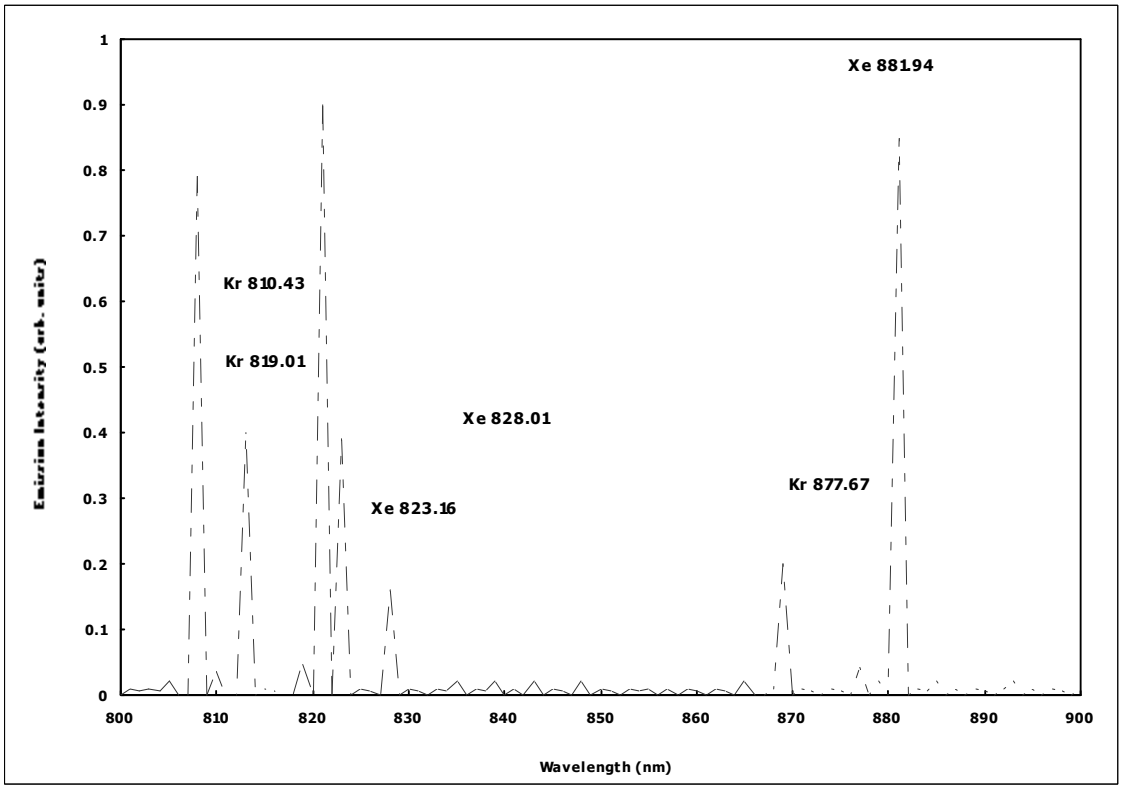

Fig. (1) Optical emission spectrum of a 0.018Torr Cl_2–Ar (1% Ar) ICP plasma at 760W RF power with 5% of the trace rare gas mixture, from 795nm to 830nm and from 865nm to 890nm. The labeled rare gas emission lines are: Kr (810.43, 819.01, and 877.67nm) and Xe (823.16, 828.01, and 881.94nm)

3. Results and Discussion

Figure (1) shows a part of the spectrum of Ar, Kr, and Xe emission lines at ~760Wfor a 1%Ar Cl_2–Ar plasma. These and other Kr and Xe emission lines are used in the TRGOES model [13] to determine T_e as a function of RF power and Ar fraction.

The model assumes a Maxwellian electron energy distribution function (EEDF) ($dn/d\varepsilon$) for electronic energies, ε, mainly in the range 9.8 to ~15eV given by:

$$\frac{dn}{d\varepsilon} = \frac{2n_e}{\sqrt{\pi}} \cdot \frac{1}{(KT_e)^{3/2}} \cdot \sqrt{\varepsilon} \exp\left(\frac{-\varepsilon}{KT_e}\right) \quad (1)$$

where n_e is electron density. This relation is used to determine the best match between the observed and computed emission intensities of the rare gases, with T_e as the only adjustable parameter. All previously reported measurements of T_e by the TRGOES technique (in chlorine and oxygen-containing plasma) have used Ar, Kr, and Xe lines [13,17,18]. When $n_g(T_g)r/T_g^{1/2}$ (n_g is the gas density, r the optical path length~reactor radius, and T_g the gas temperature) exceeds ~5×10^{11}cm^{-2} K^{-1} [19] as it does in this study for Ar fractions exceeding 1%, Ar emission in the <200 nm wavelength range is reabsorbed by the Ar atoms. This radiation trapping causes repeated excitation of energy levels above the excited states ($2p_x$ Paschen levels, x=1–10) that eventually decay to the $2p$ levels, with emission occurring at each of the Ar wavelengths (750.4, 751.5nm, etc.), resulting in enhanced emission intensities. One can either correct for this effect [19], or not use Ar emission and determine T_e over the narrower range of energies sensed by Kr and Xe emission, resulting in a somewhat degraded accuracy.

Figure (2) plots T_e versus Ar fraction at a fixed power of 600W (a real power density of 10.6W.cm^{-2}, volume power density of 0.7W.cm^{-}

^{3}), with T_e determined by using either the Kr and Xe lines only or the Kr, Xe, and Ar lines (corrected for radiation trapping of Ar emission, as described elsewhere [19]). The error bars for each datum point are from uncertainties in the parameters in the model. For a Cl_2 plasma with the 5% TRG mixture added (only ~1% Ar) both techniques should be accurate, and they both yield an electron temperature of ~4.7±0.7eV. Given the excellent agreement, it seems reasonable to use only the Kr and Xe lines to determine T_e as a function of RF power and Ar fraction.

For higher Ar fractions, where radiation trapping becomes significant, Figure (2) shows that using the Ar, Kr, and Xe lines consistently determines an electron temperature ~1eV higher than that computed using only the Kr and Xe lines. This could be real, an indication of an increase in ‘‘temperature’’ of electrons with energies ~13eV and a few eV higher at high Ar fractions, or it could be due to an underestimate of the radiation trapping effect. Refinements in the TRG-OES model would be needed to resolve this minor issue.

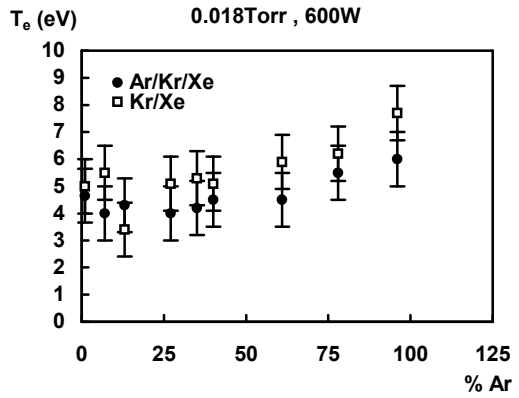

Fig. (2) Electron temperature (T_e) versus Ar fraction at 600W RF power in a 0.018Torr Cl_2–Ar ICP plasma with 5% of the trace rare gas mixture. The electron temperature is computed using either the Kr and Xe lines only or the Ar, Kr, and Xe lines

All determination of T_e is done without using Ar emission lines. Figure (2) shows that T_e increases from ~4.0±0.5eV for a Cl_2 plasma (1% Ar) to ~6.0±2.0 eV for an Ar plasma (96% Ar), with the biggest changes occurring for Ar fractions exceeding 40%. This factor of ~1.6 increase in T_e can be understood by examining the fundamental particle balance equation for an electropositive plasma (Ar, or a highly dissociated Cl_2 plasma) [20] where

$$T_e = \frac{E_{act}}{Ln(\frac{A_o n_g d_{eff}}{\nu_B(T_e)})} \qquad (2)$$

where n_g is the gas density, d_{eff} an effective ion diffusion length (4.2 and 4.3 cm for Cl^+ and Ar^+, with ion mean free paths λ_i of 1.8 and 1.7cm, respectively), ν_B ($=\sqrt{eT_e/M_i}$) the speed of positive ions as they enter the plasma sheath, and M_i the ion mass. E_{act} and A_o are the activation energy and pre-exponential factor, respectively, in the Arrhenius expression for the ionization rate constant of the neutrals. It has been shown that, $n_{Cl} >> n_{Cl_2}$ at 600W for all Ar fractions [1], so Cl and Ar are the dominant neutrals in the plasma determining T_e.

The ionization rate constants for Cl [18,21] and Ar [22] are given by the following equations:

$$k_{iz}(Cl) = 7.56\times10^{-8}.\exp(\frac{-13.74}{T_e}) \quad cm^3 s^{-1} \ (3)$$

$$k_{iz}(Ar) = 7.93\times10^{-8}.\exp(\frac{-19.20}{T_e}) \quad cm^3 s^{-1} \ (4)$$

The small difference in A_o, M_i (35.5 versus 40.0amu) and λ_i between Cl^+ and Ar^+ implies that differences in these parameters contribute negligibly to any change in T_e when the mixture is changed. By the same token, the gas density, n_g, is probably similar in Cl_2 and Ar plasmas. The temperature of a comparable Cl_2 plasma was found to be about twice that of an Ar plasma at the same power [23] halving the number density. This is roughly canceled by a doubling of the number density in the highly dissociated Cl_2 plasma. On the other hand, E_{act} is 19.20eV for Ar, compared to 13.74eV for Cl. This 5.46eV increase in E_{act} ought to increase T_e by a factor of ~1.4, in good agreement with the measured factor ~1.660.23 increase in T_e as the plasma changes from being Cl dominant (1% Ar) to Ar dominant (96% Ar). The absolute T_e computed from Eq. (2) is 4.0eV for an Ar plasma. This value is low, but nearly within the uncertainty of the measurement.

Figure (3) shows T_e as a function of RF power for different Ar fractions. T_e increases with RF power for all Ar fractions. From 350W to 750W it increases relatively little for chlorinerich plasmas, from ~3.8eV to 4.0eV for 1% Ar and from ~4.5eV to 4.6eV for 13% Ar, and by much larger factors (~1.75) for bigger Ar fractions, from ~3.5eV to 5.0eV for 40% Ar and ~4.0eV to 7.3eV for 78% Ar. The increase in T_e with RF power has been observed previously [24] and can be compared with the predicted behavior using Eq. (2). For the 95% Cl_2 discharge (1% Ar), we have shown1 that percent dissociation of Cl_2 increases from ~60% to 86% from 350W to 750W, thereby increasing n_g by a factor of ~1.45 (from ~6.6cm^{-3} to ~9.631014cm^{-3}, including estimates of the effect of gas heating [23]). This increase in n_g would decrease T_e by a factor of ~1.2. However, this is balanced by other effects of the dissociation of Cl_2 in generating species of higher ionization activation

energy E_{act} (13.74eV for Cl [18,21] versus 13.34eV for Cl_2 [18,25] and smaller ionization pre-exponential factor A_o ($7.56x10^{-8}cm^3\ s^{-1}$ for Cl [18,21] versus $1.18x10^{-7}\ cm^3\ s^{-1}$ for Cl_2 [18,25]. Together, these last two differences would increase T_e by a factor of ~1.26. The net effect is a negligible increase in T_e by a factor of ~1.05 over this power range for both the 1% and 13% Ar fractions, consistent with the experimental findings.

In contrast, for the larger Ar fractions (40% and 78%), the gas dissociation is nearly complete (~90%) for RF powers >450W [1], presumably because of the increase in T_e with Ar fraction (Fig.2). While the change in n_g with power due to dissociation is not important in determining T_e, the change in n_g with power due to gas heating still is. For the 78% Ar Cl_2–Ar discharge, we have shown1 that $n_{Cl} + n_{Cl_2}$ decreases by only ~1.1 from $3.1x10^{14}cm^{-3}$ to $2.8x10^{14}cm^{-3}$ over the RF power range investigated, while the Ar density decreases by a factor of ~2.4 from $4.5x10^{14}cm^{-3}$ to $1.9x10^{14}cm^{-3}$, based on an assumed linear rise in T_g from 300K (350W) to ~1000–1200K (800W) [23,26]. Using Eq. (2), the decrease in the net gas density, n_g ($\approx n_{Cl_2} + n_{Cl} + n_{Ar}$), ought to increase T_e by a factor of ~1.30, which is somewhat less than the factor of ~1.75 increase observed under these conditions. The Cl_2-containing plasmas are largely heated by the kinetic energy released into Cl-atoms following the dissociation of Cl_2. Consequently, the ~40% increase in T_e with increasing power in 96% Ar plasmas is even harder to explain, given the smaller temperature rise expected under these conditions. Perhaps T_g is even higher, ~2000–2500K, at higher RF powers (~750W) than the assumed values from a larger ICP system studied previously [23]. Equivalent RF powers coupled into this larger ICP system and the system used in this study corresponds to a factor of ~3 larger power density for the reactor used in this study versus that of the larger ICP system in Ref. 24 and a probable factor of ~1.7 increase in the above assumed values of T_g in the ICP used in this study [23].

4. Conclusions

Electron temperatures representative of the high-energy tail (>9.8eV) of the EEDF were measured in Cl_2–Ar ICPs by TRG-OES. Only the Kr and Xe emission lines were used to determine T_e, because of radiation trapping when the Ar emission lines were also used for larger Ar fractions. At 600W, T_e increases with Ar fraction from ~4.0±0.5eV for a (1% Ar) Cl_2 discharge to ~6.0±2.0eV for a (96% Ar) Ar discharge, due to the larger ionization activation energy of Ar (19.20eV) versus that of Cl (13.74eV). T_e is ~4.0eV and relatively independent of RF power (~350W to 750W) for the lower Ar fractions (1% and 13%) and is strongly dependent on power for larger Ar fractions, increasing from 3.5eV to 5.0eV (40% Ar) and 5.0eV to 7.3eV (96% Ar) over the same power range. Most of this can be explained by the reduction in number density due to gas heating, combined with the change in composition of chlorine-containing plasmas (Cl_2 dissociation into 2Cl) with increasing power.

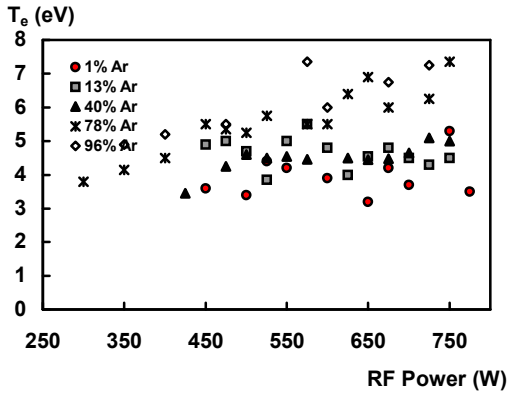

Fig. (3) Electron temperature (T_e) versus RF power and Ar fraction (1%, 13%, 40%, 78%, and 96%) in a 0.018Torr Cl_2–Ar ICP plasma with 5% of the trace rare gas mixture

Acknowledgment

The author would like to thank Professor K. Narayan (*Dept. of Physics, Indian Inst. of Technology, India*) for his supervision for this work. Also, Dr. U.A. Yajnik (*Dept. of Physics, Indian Inst. of Technology, India*) is appreciated for his discussions. This work is a part of the author's doctoral thesis and it was carried out at the Department of Physics, Indian Institute of Technology, Mumbai, India

References

[1] N. C. Fuller, V. M. Donnelly, and I. P. Herman, *J. Appl. Phys.*, 90, 3182 (2001).
[2] C. R. Eddy, Jr., et al., *J. Vac. Sci. Technol.*, A 17, 38 (1999).
[3] R. J. Shul et al., *J. Vac. Sci. Technol.*, A 14, 1102 (1996).
[4] Y. Hahn et al., *J. Vac. Sci. Technol.,* A 17, 768 (1999).
[5] R. J. Shul et al., *J. Vac. Sci. Technol.,* A 15, 633 (1997).
[6] F. Ren et al., *Appl. Phys. Lett.*, 67, 2497 (1995).
[7] J. W. Lee et al., *J. Vac. Sci. Technol.*, A 14, 2567 (1996).
[8] T. Fujiwara et al., *Jpn. J. Appl. Phys.*, Part 1, 33, 2164 (1994).
[9] S. Samukawa et al., *Jpn. J. Appl. Phys.*, Part 1, 34, 6805 (1995).

[10] S. Samukawa, *Jpn. J. Appl. Phys.*, Part 1, 33, 2133 (1994).
[11] T. Hori et al., *J. Appl. Phys.*, 83, 1909 (1998).
[12] T. Hori et al., *Appl. Phys. Lett.*, 69, 3683 (1996).
[13] M. V. Malyshev and V. M. Donnelly, *Phys. Rev. E*, 60, 6016 (1999).
[14] J. Y. Choe, I. P. Herman, and V. M. Donnelly, *J. Vac. Sci. Technol.*, A 15, 3024 (1997).
[15] J. M. Lafferty, "**Foundations of Vacuum Science and Technology**", Wiley (NY) (1997), 53–54.
[16] F. O'Hanlon, "**A User's Guide To Vacuum Technology**", Wiley (NY) (1989), 22.
[17] N. C. Fuller et al., *Plasma Sources Sci. Technol.*, 9, 116 (2000).
[18] V. M. Donnelly et al., J. I. Colonell, and J. T. C. Lee, *Jpn. J. Appl. Phys.*, Part 1, 37, 2388 (1998).
[19] M. Schabel, V. Donnelly, A. Kornblit, and W. W. Tai, *unpublished results, private communications*.
[20] M. A. Lieberman and A. J. Lichtenberg, "**Principles of Plasma Discharges and Materials Processing**", Wiley (NY) (1994), 306.
[21] T. R. Hayes, R. C. Wetzel, and R. S. Freund, *Phys. Rev. A*, 35, 578 (1987).
[22] H. C. Straub et al., *Phys. Rev. A*, 52, 1115 (1995).
[23] M. V. Malyshev and V. M. Donnelly, *Appl. Phys. Lett.*, 77, 2467 (2000).
[24] M. V. Malyshev and V. M. Donnelly, *J. Appl. Phys.*, 87, 1642 (2000).
[25] F. Stevie and M. J. Vasile, *J. Chem. Phys.*, 74, 5106 (1981).
[26] Reference 21 determined a square root dependence of gas temperature with RF power but since this dependence may be very reactor specific and the power density in this reactor is ~3X that in Ref. 21, a linear dependence was assumed here.

This article was reviewed at Department of Science and Engineering, Nagasaki University, JAPAN and School of Applied Sciences, University of Technology, Baghdad, IRAQ

Coming Conferences and Symposia

7TH WORKSHOP ON INFORMATION OPTICS
1–5June 2008
Annecy, France
http://wio2008.univ-st-etienne.fr/

MRS INTERNATIONAL MATERIALS RESEARCH CONFERENCE
(selected symposia)
9–12 June 2008
Chongqing, China
http://www.mrs.org/s_mrs/sec.asp?CID=7060&DID=178708

INTERNATIONAL WORKSHOP 60 YEARS OF CASIMIR EFFECT
23–27 June 2008
International Center of Condensed Matter Physics, Brasilia, DF, Brazil
http://www.iccmp.web.br.com/en/evento_19.php

2ND NATIONAL CONFERENCE ON NANOTECHNOLOGY "NANO 2008"
25–28June 2008
Jagiellonian University, Krakow, Poland
http://confer.uj.edu.pl/nano2008/index.php?(=en

"DUBNA-NANO2008" INTERNATIONAL CONFERENCE ON THEORETICAL PHYSICS
7–11 July 2008
Dubna, Moscow Region, Russia
http://theor.jinr.ru/~nano08

SCIENTIFIC DISCOVERY THROUGH ADVANCED COMPUTING 2008 (SCIDAC 2008)
13–17 July 2008
Fairmont Olympic Hotel, Seattle, Washington, USA
http://hpcrd.lbl.gov/SciDAC08/SciDAC.html

25TH INTERNATIONAL CONFERENCE ON LOW TEMPERATURE PHYSICS (LT25)
6–13 August 2008
Amsterdam, Netherlands
http://www.lt25.nl/

THE 13TH INTERNATIONAL CONFERENCE ON RAPIDLY QUENCHED AND METASTABLE MATERIALS
24–29 August 2008
Dresden, Germany
http://rq13.ifw-dresden.de/

14TH INTERNATIONAL CONFERENCE ON THE PHYSICS OF HIGHLY CHARGED IONS
1–5 September 2008
Chofu City Culture Hall "Tazukuri", Chofu, Tokyo, Japan
http://yebisu.ils.uec.ac.jp/hci2008

16TH INTERNATIONAL SYMPOSIUM ON BORON, BORIDES AND RELATED MATERIALS
7–12 September 2008
Matsue, Shimane, Japan
http://www.sogalabo.jp/ISBB2008/

INTERNATIONAL WORKSHOP ON STATISTICAL-MECHANICAL INFORMATICS 2008 (IW-SMI 2008)
14–17 September 2008
Aobayama, Aoba-ku, Sendai 980-0856, Japan
http://dex-smi.sp.dis.titech.ac.jp/DEX-SMI/iw-smi2008/

INHALED PARTICLES X
23–25 September 2008
Manchester University, UK
http://www.bohs.org/newsArticle.aspx?newsItem=61

Iraqi J. of Appl. Phys. , Vol. 4 , No. 1 , 2008 , 11-14

Design of a Fundamental Concept of Virtual Reality System for Intensity Distribution in Free Electron Laser Amplifier

Haider M. Daoud [1]
Mohammad I. Sanduk [1]
Mohammad Z. Al-Faiz [1]
Raad A. Khamis [2]

[1] *Department of Laser Engineering, Faculty of Engineering, Al-Nahrain University, Baghdad, Iraq*
[2] *School of Applied Sciences, University of Technology, Baghdad, Iraq,*
drraad2001@yahoo.com

Special algorithm for FEL amplifier at saturation effects were dedicated to visualizing intensity distribution in planar undulator depending on one-dimension FEL amplifier theory. This efficient algorithm for FEL Simulation Code has been applied to study the field gain distribution along the undulator length to explain high gain FEL operating mechanism in nonlinear regime.

Keywords: *Non-linear Simulation, Virtual Reality, FEL Process*
Received 4 September 2006, Revised 20 March 2008, Accepted 25 March 2008

1. Introduction

The Free-Electron Laser process is the interaction between an electron beam and a co-propagating radiation field, resulting in a collective instability with an exponential growth of the radiation field and the current modulation in the electron bunch. Although analytical models can describe the fundamental FEL amplification, the complexity of the FEL process with a multi-particle system and the evolution of a radiation field demands numerical calculation [1].

To achieve optimum performance, the numerical solver for FEL code is highly specialized. This paper describes the basic algorithm for FEL simulation and addresses in particular the problems and limitations of simulating the FEL process.

2. Algorithm Structure of FEL Amplifier at Saturation Effects

In the linear mode of FEL amplifier, the operation mechanism is presenting when an increase of the input power (W_{ext}) leads to a proportional increase of the output power (W_{out}). When the input power is increased further, the operation of the amplifier becomes nonlinear: the output power increases more slowly than the input power, and at a certain value of W_{ext}, the output power reaches a maximum [2].

For simulation model of High Gain FEL operating mechanism, it is possible to consider the beam as coming from a "black box" and ignore the details of the accelerator, beam optics and diagnostics (see Fig. 1). For the purposes of this work, a beam is a collection of relativistic particles (usually electrons), and an undulator is a device that produces a periodic magnetic field. The operating definition is that a FEL is a device which produces coherent (or partially coherent) radiation from an electron beam by extracting energy from the beam through a stimulated emission process [3,4].

3. FEL Amplifier with a Planar Undulator

Let us now demonstrate the characteristics calculation of the FEL amplifier with planar undulator in the case of linearly polarized radiation. The equations of motion of the electrons in the field of the planar undulator can be obtained by using the Hamiltonian formula written down in terms of the energy-phase variables $P = \varepsilon\text{-}\varepsilon_o$ and the canonically conjugate phase $\psi = k_w z + \omega(z/c - t)$ [1].

In the case of little influence of the space charge field, the equation of motion have the form [5]:

$$\frac{\mathrm{d}P}{\mathrm{d}z} = iU\exp(i\psi) + C.C. \qquad (1)$$

$$\frac{\mathrm{d}\psi}{\mathrm{d}z} = C + \frac{\omega\theta_\ell^2}{4c}\cos(2k_w z) + \frac{\omega P}{c\gamma_\ell^2\varepsilon_o} \qquad (2)$$

where k_ω is the wavenumber of the undulator, z is the Cartesian coordinate, γ_ℓ is the longitudinal relativistic factor in planar undulator, ω is a frequency of the amplified electromagnetic wave, $C = k_w + \omega/(c\gamma_\ell^2\varepsilon_o)$ is the detuning of the electron with the nominal energy ε_o, and $U = -\left[1-\exp(-2ik_w z)\right]e\theta_\ell\widetilde{E}_x(z)/2$ is the

complex amplitude of the effective potential, θ_ℓ is maximal angle of electron oscillation in a planar undulator.

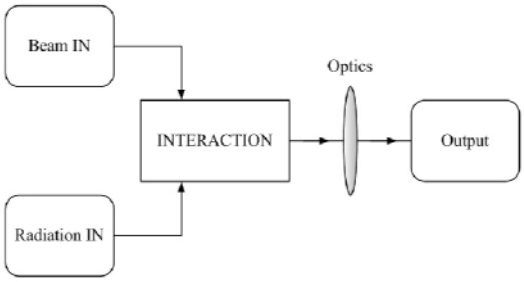

Beam Input	Includes user input detailing the beam's initial *n*-dimensional phase space (i.e., energy spread, particle distribution model, prebuncher, etc.).
Radiation Input	Contains parameters such as the power, and wavelength, and information on how the startup should be modeled (i.e., whether it is spontaneous or from a coherent source).
Beam Radiation Interaction	It is actually the FEL equation solver.
Optics	Section allows for feedback or manipulation of the output radiation to better model experimental realities (such as a long drift of the radiation to a far away detector).
Output	Section provides numerical versions of radiation and beam diagnostics as well as graphics support.

Fig. (1) A simplified block diagram of a single–pass FEL. The "radiation in" box represents either a coherent input source or the effective start-up power from spontaneous emission.

The complex amplitude of the amplified wave can be written as [5]:

$$\frac{\mathrm{d}\widetilde{E}_x}{\mathrm{d}z} = -i\pi\theta_\ell c^{-1}\left[\exp(2ik_w z)-1\right]\widetilde{j}_1(z)$$

where $\widetilde{j}_1(z)$ is the complex amplitude of the first harmonic of the beam current density.

Then, we choose the new definition of the phase:

$$\psi' = \psi - Q\sin(2k_w z) \tag{3}$$

Therefore, the equations of motion and the field equation can rewrite in terms of the new phase ψ' and averaging over the undulator period,

$$\frac{\mathrm{d}P}{\mathrm{d}z} = \frac{-i}{2}A_{JJ}\,e\theta_\ell\,\widetilde{E}_x\exp(i\psi) + C.C. \tag{4}$$

$$\frac{\mathrm{d}\psi'}{\mathrm{d}z} = C + \frac{\omega P}{c\gamma_\ell^2\varepsilon_o} \tag{5}$$

$$\frac{\mathrm{d}\widetilde{E}_x}{\mathrm{d}z} = i\pi A_{JJ}\,\theta_\ell c^{-1}\widetilde{j}_a \tag{6}$$

where $A_{JJ}=[J_0(Q)-J_1(Q)]$ and $\widetilde{j}_a(z) = \widetilde{j}_1(z)\exp[iQ\sin(2k_w z)]$

The next step considers in writing down the equations in reduced form, we perform the normalization procedure as [4]:

$$\hat{z} = \Gamma z\ ,\ \hat{P} = P/(\rho\varepsilon_o)\ ,\ \hat{C} = \Gamma/C$$

$$\hat{u} = u/(\rho\varepsilon_o\Gamma) = \left|\widetilde{E}_x\right|/E_0 \tag{7}$$

where u is amplitude of the effective potential, $\rho = c\gamma_\ell^2\Gamma/\omega$ is efficiency parameter in FEL amplifier theory,

$$\Gamma = \left[\frac{\pi\theta_\ell^2 j_o\,\omega A_{JJ}^2}{2c\gamma_\ell^2\gamma I_A}\right]^{1/3} \text{ and}$$

$$E_o = \left[\frac{c\varepsilon_o\gamma_\ell^2\Gamma^2}{e\,\gamma_\ell\,\omega A_{JJ}}\right] \text{ is saturation field}$$

amplitude parameter.

As a result, we can write the self-consistent equations in the following reduced form [4]:

$$\frac{\mathrm{d}\hat{P}}{\mathrm{d}\hat{z}} = \hat{u}\cos(\psi'+\psi_o) \tag{8a}$$

$$\frac{\mathrm{d}\psi'}{\mathrm{d}\hat{z}} = \hat{P} + \hat{C} \tag{8b}$$

$$\frac{\mathrm{d}\hat{u}}{\mathrm{d}\hat{z}} = \hat{j}_a\cos(\psi_o-\psi_a) \tag{9a}$$

$$\frac{\mathrm{d}\psi_o}{\mathrm{d}\hat{z}} = -(\hat{j}_a/\hat{u})\sin(\psi_o-\psi_a) \tag{9b}$$

where $(\hat{u},\psi_o)$ and $(\hat{j}_a,\psi_a)$ are related to the complex amplitude $\widetilde{E}_x$ and $\hat{j}_a$ by the following expressions [5]:

$$\hat{u}\,e^{i\psi_o} = -i\widetilde{E}_x/E_o \qquad \hat{j}_a\,e^{i\psi_o} = 2\widetilde{j}_a/j_0$$

The equation of motion (8) and the field equation (9) form a system of 2*N*+2 equations describing the amplification process in the FEL amplifier.

4. Field Amplitude Saturation in the High-Gain FEL Amplifier

Equations (8) and (9) form a system of self-consistent equations describing the nonlinear mode of FEL amplifier operation. For initial conditions, which are typically small initial radiation fields and a nearly un-bunched beam, the start-up of the amplification can be described by the FEL equations in the linear regime which have been discussed in references [1, 4].

The general solution is a sum of several independent modes which are either oscillating, decaying, or growing. The initial amplitudes of these modes are of the same order of magnitude and exhibit interference till the exponential growing mode dominates.

There are two interesting regimes shown in Fig. (2). The *lethargy*, or *start–up* regime that occurs at the beginning of a FEL where the instability (the growing exponential) has not yet dominated the decaying exponential and the linear terms. Saturation occurs when the nonlinear forces damp the instability. In reality, the saturation length is dependent on the FEL

parameter, and the number of gain lengths within the saturation length can vary depending on the device. The effective parameters, which can be specified in our numerical and simulation treatments, are the relation between the phase of the effective potential of particle wave interaction (ψ_o) and phase of the first harmonic of the longitudinal component of the beam current density (ψ_1).

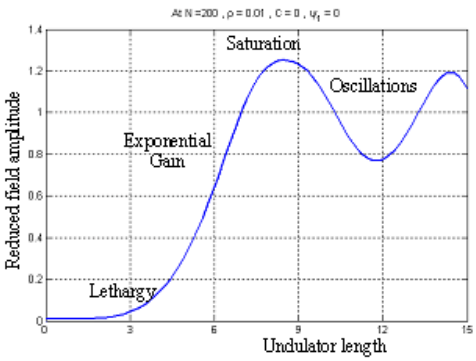

Fig. (2) Reduced field amplitude versus reduced length of the undulator, showing the start–up from a small input signal (lethargy), the exponential growth, and saturation

The difference between ψ_o and ψ_1, which is denoted by $\delta\psi$, can be described by the dynamical relation between the complex amplitude of the electron field ($\tilde{E}$) and the amplitude of the first harmonic of the longitudinal component of the beam current density j_1 along the undulator length z. We can diagnose the collective effects in the normalized amplitude of the effective potential ($\hat{u}$) for several values of $\delta\psi$ along the reduced undulator length ($\hat{z}$).

We consider the initial conditions when the electron beam is neither modulated in velocity nor in density and there is an electromagnetic wave of amplitude E_{ext} at the undulator entrance at $z = 0$ (j=1, 2, … ,N):

$$\hat{P}_{(j)}(0) = 0\,,\ \hat{j}_1(0) = 0\,,\ \hat{u}(0) = \hat{u}_{ext} = E_{ext}/E_o$$

According to equation (**4.26**), the saturation field parameter is given by

$$E_o = \rho\varepsilon_o\Gamma/e\theta \qquad (10)$$

We start with the simplest process on the operation of the FEL amplifier. The plots in figures (3-5) illustrate the dependence of the reduced field amplitude ($\hat{u}$) on the reduced undulator length ($\hat{z}$) for $\hat{C} = 0$ and $\hat{u}_{ext} = 0.01$.

In Fig. (3), the behavior of field is of the same activity as the field for linear regime where the electron bunches, which will be discussed in the next section, do not appear.

However, the field stops growing at the saturation point when the beam is over-modulated and a significant fraction of the electrons falls into accelerating phase of the effective potential (see Fig. 4).

When the value of $\delta\psi$ is equal to 0.0° at ψ_1=90°, the field falls at the undulator entrance to increase its value, and still oscillating along the undulator length. This phenomenon is shown in Fig. (5).

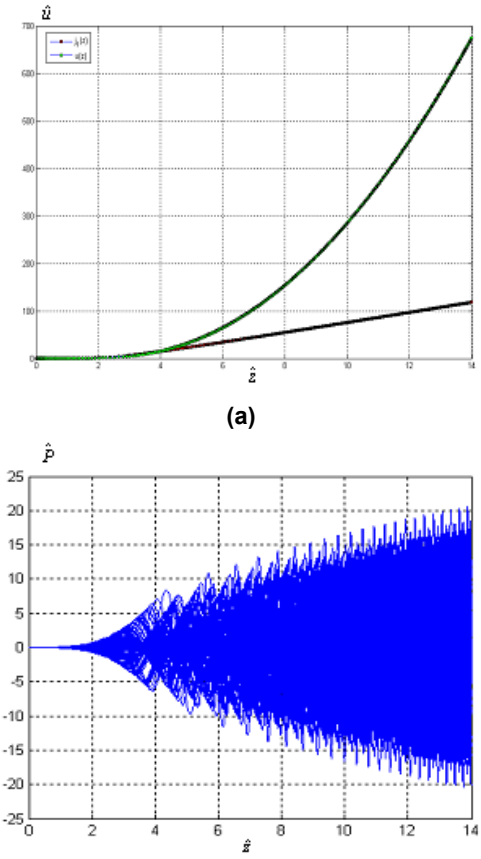

Fig. 3 Simulation Results of FEL Amplifier for Non-Linear Regime at $\delta\psi$ = 10°, ψ_1=10° and $\hat{C}$ = 0 (a) Reduced field amplitude versus reduced undulator length and (b) Reduced canonical momentum versus reduced undulator length

This calculation scheme of the FEL amplifier output characteristics in saturation mode (non-linear regime) which is suitable for engineering practice is presented in this work. This scheme stems from similarity techniques and numerical simulation results given as design formulae and universal plots.

5. Conclusions

Our Free Electron Laser Simulation Code (FELSC) has to fill the gap of analytical treatment that provide fast results and which cannot cover the entire complex system of the Free-Electron Lasers. Where the rigorous results obtained in deduced form furnish universal plots for calculating the output characteristics of the FEL amplifier in the linear mode of operation.

These analytical solutions serve as a reliable basis for the development of numerical methods. The analysis of nonlinear process refers to problems solvable only numerically by a computer. On the other hand, testing of the numerical simulation codes would be difficult without the use of rigorous results of FEL amplifier linear theory as a primary standard.

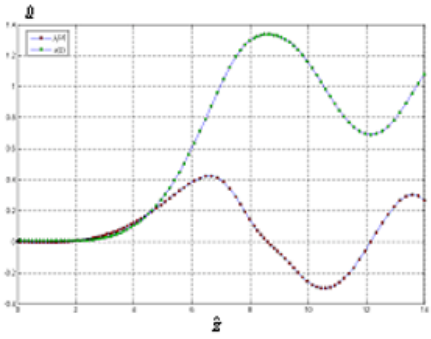

(a)

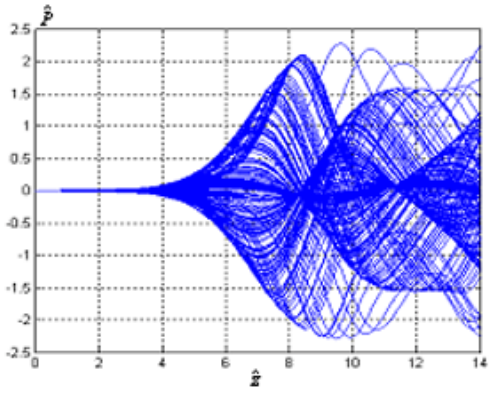

(b)

Fig. 4 Simulation Results of FEL Amplifier for Non-Linear Regime at $\delta\psi$=46.5°, ψ_1=46.5° and $\hat{C}$=0 (a) Reduced field amplitude versus reduced undulator length and (b) Reduced canonical momentum versus reduced undulator length

References

[1] W. B. Colson, **"Fundamental Free Electron Laser Theory and New Principles for Advanced Devices,"** SPIE vol. 738, pp. 1-27, 1978.

[2] H. M. Duoud, M. Z. Al-Faiz, M. I. Sanduk and R. A. Khamis, "Extraction the General Solution of Integro-Differential Equation in a Mono-Energetic Electron Beam Case," to be published in Journal of the Institute of Electrical & Electronics Engineers (IEEE–Jordan), 2005.

[3] G. Travish, "Experimental Requirements for a Self-Amplified Spontaneous Emission Test System: Design, Construction, Simulation and Analysis of the UCLA High Gain Free Electron Laser," Ph.D. thesis, University of California, Los Angeles, 1996.

[4] H.M. Daoud, "Design a Virtual Reality System of Electron Beam Bunch Distribution in Free Electron Laser," Ph.D. Thesis, Al-Nahrain University, Baghdad, 2005.

[5] E.L. Saldin, E.A. Schneidmiller and M.V. Yurkov, **"The Physics of Free Electron Lasers"**, 1st edition by Springer-Verlag Berlin Heidelberg, 2000.

[6] R.A. Khamis, H.M. Daoud, M.Z. Al-Faiz, and M.I. Sanduk, "Study the Integro-Differential Equation in a Lorentzian Energy Spread Case," to be published in *J. Eng. Technol.*, Baghdad, 2006.

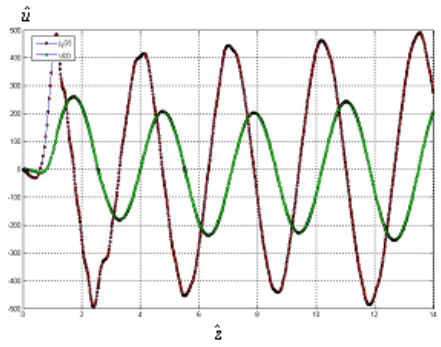

(a)

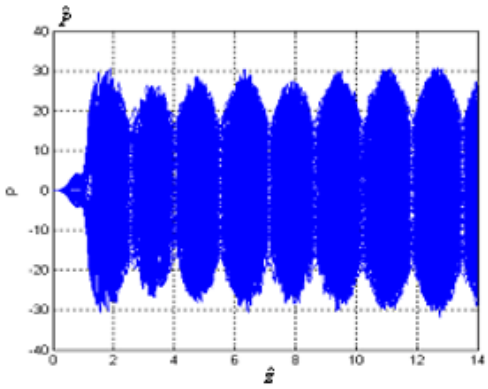

(b)

Fig. 5 Simulation Results of FEL Amplifier for Non-Linear Regime at $\delta\psi$= 0.0°, ψ_1=90° and $\hat{C}$=0 (a) reduced field amplitude versus reduced undulator length and (b) reduced canonical momentum versus reduced undulator length

This article was reviewed at Department of Physics and Astronomy, University of Vanderbilt, USA, School of Physics, Duke University, UK, and School of Applied Physics, University of Technology, Baghdad, IRAQ

BIOSENSORS
Technology & Applications

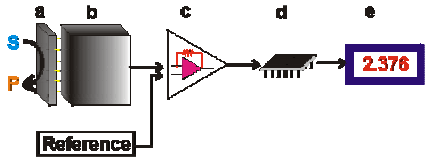

Written by
Walid K. Hamoudi *(professor)*
School of Applied Science
University of Technology, Baghdad, IRAQ

A biosensor is a powerful analytical device which converts a biological response into an electrical signal in order to determine the concentration of substances and other parameters of biological interest even when no biological systems are utilized directly. Biosensors represent a rapidly expanding field, at the present time, with an estimated 60% annual growth rate; the major imput coming from the health-care industry (e.g. 6% of the western world are diabetic and would benefit from the availability of a rapid, accurate and simple biosensor for glucose) but with some pressure from other areas, such as food quality appraisal and environmental monitoring. Within the food and beverage industries, it is increasingly a priority to be able to measure and control flavor and achieve the desired outcome.

The estimated world analytical market is about $24,000,000,000 per a year of which 30% is in the health care area. There is clearly a vast market expansion potential as less than 0.1% of this market is currently using biosensors. By interfacing three advanced technologies: nanomaterials, biomaterials and electronic transducers, we will have the ability to create enhanced biosensors and nanobioelectronics. Research and development in this field is wide and multidisciplinary, spanning biochemistry, bioreactor science, physical chemistry, electrochemistry, electronics and software engineering. In the following biosensor schematic below; the biocatalyst (a) converts the substrate to product. This reaction is determined by the transducer (b) which converts it to an electrical signal. The output from the transducer is amplified (c), processed (d) and displayed (e).

Biosensors have the ability to measure constantly the presence, absence, or concentration of specific organic or inorganic substances and to do so accurately, with rapid response time and low cost. Their advantages over existing technologies include the ability to monitor broad or narrow spectra of analyses continuously in real time and simply to allow decentralized analyses testing. Their weakness however is in their shelf life due to the instability of the biological molecules outside their natural environment.

Commercial applications of biosensors are mainly in the areas of health care, food-quality control, pharmaceuticals, and environmental monitoring. A common requirement of all these applications is on-site analysis, preferably on a real-time basis. The resulting benefits of closer monitoring range from a more efficient industrial productions process to better safety standards of chemical and biological hazards. However, the market demand for employing biosensors will accelerate only when cheap and reliable biosensor technologies become available. The apparent opportunities in biosensor commercialization have led to interest by many large electronic and life science

companies but, without the technical skills, the users will have great difficulty entering the market.

Bottlenecks in the technical development of biosensors include the difficulty of fabricating devices in bulk and the single- or restricted multiple-use nature of most biosensors currently available. In addition, the combination of electronic and biological components in a working device is currently difficult and expensive to achieve and requires significant class-discipline research. The high cost of biosensor development reduces the potential for biosensor use in low-cost applications. Because several competing technologies to biosensors exist, the commercial success of biosensors hinges on their use in applications where they have a unique performance advantage such as simplicity of use, greater sensitivity, faster response time, or the ability to monitor analyses continuously. Even in the largest markets (such as glucose monitoring) that biosensors can access, competition on price or technology alone is unlikely to form the basis of a successful strategy.

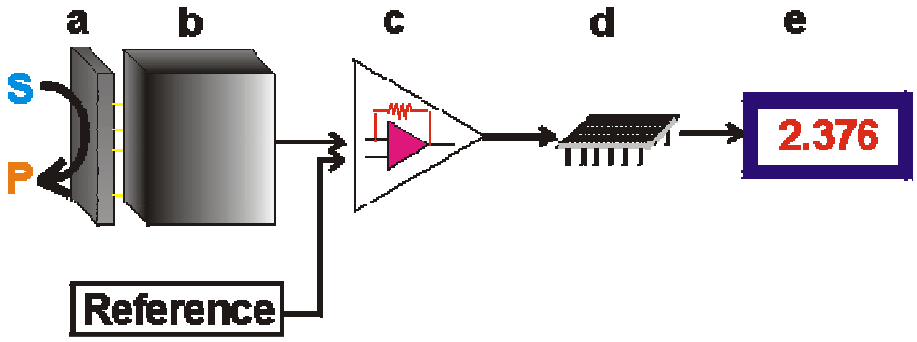

References:

1- "Biosensors" SRI Consulting Business Intelligence, Report by Rob Reid.

2- "What are Biosensors?" London South Bank University, Faculty of Engineering, Science and the Built Environment.

3- "Biosensors" Center for Bioelectronics and Biosensors web page.

4- "Biosensors – Innovative Patient Diagnostics" Oxford Biosensors Brochure.

"Quality Biosensors" Commonwealth Scientific and Industrial Research Organization, Australia's National Science Agency.

Iraqi J. of Appl. Phys. , Vol. 4 , No. 1 , 2008 , 17-23

Methods of Determining The Refractive Index of Thin Solid Films
(Article Review)

Salwan K. Al-Ani

Department of Physics, College of Education, Seyoun-Hadhramout University for Science and Technology, Yemen
salwan_kamal@yahoo.com

Thin multilayer graded semiconducting, inorganic, metallic oxides films have wide applications such as optical designs and microelectronics industry. Knowledge of the refractive indices $n_f(\lambda)$ and of such films their dispersion are important. This paper is aimed to present an overview on the different methods that have been devised for the determination of the index of refraction of thin films along with their theoretical basis. Such methods are Abeles, Swanepoel, Kramers-Kronig, Ellipsometer, and others. Some experimental results are also presented. The accuracy of these methods is evaluated.

Keywords: *Thin films, optical properties, refractive index, interference fringes*
Received 31 January 2006, Revised 18 March 2008, Accepted 25 March 2008

1. Introduction

Thin solid films have proved a very useful vehicle to understand the properties and structure of a solid material especially in its non-crystalline form. Indeed, the determination of the value of refractive index (n_f) and its dispersion, (i.e. variation of n_f *vs.* the wavelength of the incident light (λ) of non-metallic thin solid films have wide applications in designing different optical components and modeling optical coatings. When a monochromatic electromagnatic radiation of angular frequency (ω) interacts with a material (Fig.1) the reflected, transmitted and absorbed radiation components satisfy the following conservation formula:

$$A(\omega) + R(\omega) + T(\omega) = 1 \qquad (1)$$

where A(ω), R(ω) and T(ω) are the spectral absorbance, reflectance and transmittance, respectively. All the above spectral optical properties are wavelength-dependent.

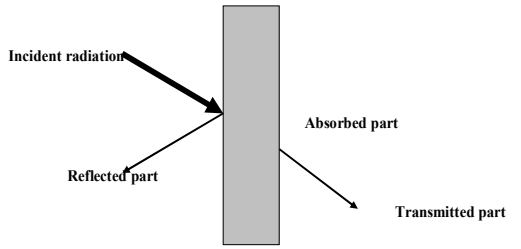

Fig. (1) The interaction of electromagnetic radiation with a material

The complex index of refraction (n_c) is defined as:

$$n_c = n - ik \qquad (2)$$

and is related to the velocity of propagation by:

$$v = \frac{c}{n_c} \qquad (3)$$

where k is the extinction coefficient *and* c is the velocity of light in vacuum.

The absorption coefficient $\alpha(\omega)$ at angular frequency of radiation (ω) is given by

$$\alpha(\omega) = \frac{4\pi k}{\lambda} \qquad (4)$$

The real dielectric constant (ε) is related to those optical constants (n, k) by the relation:

$$n^2 - k^2 = \varepsilon \qquad (5)$$

$$nk = \frac{\sigma}{v} \qquad (6)$$

where σ and v are the conductivity and frequency, respectively.

The dielectric constant (ε) may be defined as a complex:

$$\varepsilon = \varepsilon_1 + i\varepsilon_2 \qquad (7)$$

Thus

$$e_1 = n^2 - k^2 \qquad (8)$$

$$e_2 = 2nk \qquad (9)$$

In this paper different methods that have been devised for the determination of the refractive index of thin films are presented and discussed. Some experimental results are also given and evaluated.

2. Experiment

The ultraviolet, visible, near-infrared and infrared spectral optical properties measurements of thin films at near-normal incidence are usually conducted using a dual beam spectrophotometer

such as Perkin-Elmer lambda 9 or Bruker FT in the wavelength range (190-2500)nm and (2.5-50)μm. Other experimental details may be found with each method discussed below.

3. Results and Discussions

3.1 Abelés Method

The method of Abelés [1,2] to obtain the refractive index of thin films is rather simple and accurate. This method measures the Brewster angle of the film and depends on the fact that for a polarized light with its electric vector in the plane of incidence, the reflectance of the film (index n_f) deposited on a substrate (index n_s) at an angle $\tan\phi_0=n_f/n_0$ is the same as the reflectance of the bare substrate. The medium of incidence is air (n_o). Therefore, coating of the film over half the substrate is required for the measurement of the refractive index.

The only apparatus required is a spectrometer modified to achieve a telescope rotation at a twice the rate of the specimen and to be focused on this specimen instead of at infinity, and a monochromatic source of radiation.

When equal intensity of the polarized monochromatic light is reflected from the film-bare substrate, that angle of incident is noted and the refractive index of the film (n_f) is read from tangent tables. For ease and accurate measurement this method requires a phase difference $\delta=\pi$ between the incident and emerging beams.

3.1.1 Theory

For light polarized with its electric vector in the plane of incidence, the reflectance from a dielectric layer is (Fig. 2):

$$R_p = r_1^2 p = \frac{\tan^2(\phi_2 - \phi_0)}{\tan^2(\phi_1 - \phi_0)} \qquad (11)$$

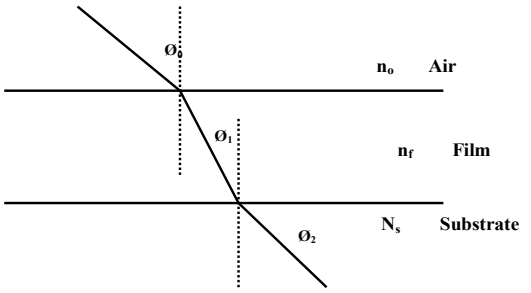

Fig. (2) The refractive index of a transparent film on a transparent substrate (Abeles method)

For transparent film and substrate and when $n_f \geq n_s$:

$$R_p = \frac{r_1^2 - 2r_1 r_2 \cos 2\delta_1 + r_2^2}{1 - 2r_1 r_2 \cos 2\delta_1 + r_1^2 r_2^2} \qquad (12)$$

where,

$$r_1 = \frac{\tan(\phi - \phi_0)}{\tan(\phi_1 + \phi_0)},\ r_2 = \frac{\tan(\phi_2 - \phi_1)}{\tan(\phi_2 + \phi_1)} \text{ and}$$

$$\delta_1 = \frac{2\pi n_1 d_1 \cos\phi_1}{\lambda}$$

For an incident angle $\tan\phi_0=n_f/n_0$, which is the Brewster angle, $\phi_0+\phi_1=90^o$. Thus, the term ($\tan 90°=\infty$) and ($r_1=0$) for the light polarized with its electric vector parallel to the plane of incidence. Therefore, $R_p=r_2^2$. Thus, the reflectance of the film-substrate is equal to the reflectance of the substrate only.

Abelés claimed an accuracy of 0.002 if the difference in refractive indices of the film and the substrate is less than 0.3. Using this method, values of n_f=1.8-2.0 were obtained for evaporated SiO thin film [3]. The variation of n_f with the parameter R/p, (where R is the rate of evaporation and p is the pressure during the evaporation process) for SiO thin films are obtained [4].

For silicon oxide film, Timson [5] and Al-Ani *et. al* [6] have found the value of n_f is 1.95-2.0 for high values of R/p which corresponds to pre-dominantly SiO whereas n_f is 1.6 for low values of R/p, which tends to the composition of SiO_2.

Fujiwara [7,8] applied Abelés method to obtain the values of n_f of different mixing ratio of two low- and high-index materials in the composite thin films.

3.2 Reflectance and transmittance Method

The utility of thin films that absorb light in the visible and infrared regions has significantly increased due to their uses in photo-thermal and photovoltaic conversion of sunlight. Therefore, thousands of papers have been reported on the optical constants (n_f and k_f) for a wide range of films.

Although the normal or near normal reflectance (R) and transmittance (T) data are available for most thin films, the processing of these data posses some difficulties because of the existence of multiple solutions for optical constants (n_f) and (k_f) which are compatible with the measured reflectance and transmittance data.

Three techniques of determining the optical constants of thin semiconducting films using normal incidence reflectance and transmittance data were described by McKenzie *et. al* [9]. One of their techniques uses the functions $F_1=(1+R)/T$ and $F_2=(1-R)/T$ rather R and T of the film directly. Values of F_1 and F_2 were first deduced from measured values of (R) [from air side of the film] and (T). Values of n_f and k_f that agree with $F_1$and F_2 over a range is obtained. The same procedure is repeated for R and T of the

substrate. Those methods have been applied to a-C, a-C: H, Si and Si:H films.

From the expressions for (1-R)/T, a procedure is given [10] for determining the correct solutions for n_f and k_f and obtaining the film thickness with the condition of a homogenous single layer film on a substrate. It has been found necessary to assume an oxide layer and make use of an equation of double layer on a substrate. Accordingly, Denton *et. al* [10] suggested coating a film with a suitable transparent layer to avoid any contamination of a film after removal from vacuum and allowing a reliable measurements of its optical constants.

3.3 Interference fringes method

Recently, the interference methods have received more attention and further improvements were introduced to increase their accuracy and simplicity. The values of n_f are in accordance with that derived from the position of the interference maxima

$$2n_f d=m\lambda \tag{13}$$

where d is the thickness of the film, which must be accurately known, and m the order of the interference. The first order interference fringe occurs at the longer wavelength.

If the order of interference (m) is not established and for adjacent maxima, Eq. (13) may be written as

$$(2n_f d) = m\lambda_m = (m+1)\lambda_{m+1} \tag{14}$$

Allowing m to be eliminated so

$$(2n_f d)^{-1} = \lambda_{m+1}^{-1} - \lambda_m^{-1} \tag{15}$$

λ_{m+1} and λ_m can be read directly from the transmission spectrum and n_f can be easily computed.

Values of the refractive index from the position of interference maxima and minima for non-metallic thin films have been reported for systems such as SiO_x, WO_3, V_2O_5, TeO_2, Se, GeO_x, Si,BaO-SiO,As_2O_5-SiO, SiO-GeO_2 [11-16].

From the optical transmission spectra in the UV-VIS-NIR regions, the transmittance maxima (T_{max}) and minima (T_{min}) at various wavelengths (λ) are read from the envelope connecting those peaks to find $n_f(\lambda)$ using Swanepoel formula [17]:

$$n_f(\lambda)=\{N+(N^2-n_s^2)^{1/2}\}^{1/2} \tag{16}$$

where $N = \frac{2n_s\{T_{\max}(\lambda)-T_{\min}(\lambda)\}}{T_{\max}(\lambda)T_{\min}(\lambda)} + \frac{(n_s^2+1)}{2}$ and n_s is the refractive index of the substrate. Further developments have been undertaken to increase the method accuracy [18-19].

Further analysis of the dispersion curves can be made from the simple dispersion theory in the low absorption where n_f is given by [20]:

$$n_f^2 - 1 = \frac{S_0\lambda_0^2}{1-\left(\frac{\lambda_0}{\lambda}\right)^2} \tag{17}$$

where λ_0 is an average oscillator position and S_0 is an average oscillator strength.

Manificier *et. al* [21] have developed more accurate method for deducing n_f and k_f from the figure pattern of the transmission spectrum provided $k^2<<n^2$. Using air as the first medium, n_f is obtained from:

$$n_f=[N+(N^2-n_s^2)^{1/2}]^{1/2} \tag{18}$$

where $N=\{(1+n_s^2)/2+[2n_s(T_{max}-T_{min})/T_{max}T_{min}]\}$.

This method has been applied for Al_xO_y thin film prepared by reactive evaporation [22]. Reasonable agreement was obtained with results reported by other techniques.

3.4 The prism spectrometer and other methods

A fundamental optics experiment is the investigation of the dispersion of visible light using a prism spectrometer.

The refractive index n_{pr} of the prism material is calculated from the familiar relation:

$$n_{pr}=\sin[(A+D_{min})/2]/\sin(A/2) \tag{19}$$

where A is the refracting angle of the prism and D_{min} is the angle of minimum deviation. This experiment is useful for understanding the meaning of refractive index and its normal and anomalous dispersion regions

Due to the dispersion relation (i.e., n v_s λ) and the Cauchy relation (n v_s λ^{-2}), for example, the refractive index of electron-evaporated Al_2O_3 films was brought into the dispersion formula [23]:

$$n(Al_2O_3) = \frac{1+1.6139\lambda^2}{\lambda^2-(124.7)^2} \quad (\lambda \text{ in nm}) \tag{20}$$

Different methods have been suggested for the measurement of n_{pr} with a (45°-45°-90°) and equilateral (60°-60°-60°) prisms [24-25].

A simple formula, however, has been used [26-27] to analyse the dispersion curve for the visible and the infrared transmitting glasses (n_g). The dispersion curves plotted for these typical IRG series glasses are in excellent agreement with those plotted using the manufacturer's (Schott) data. Also, Classic dielectric theory provides a number of relationships between refractive index and density of solids.

Correlation for glasses and thin films has been established [28-29] using Lorentz-Lorenz, Gladston-Dale and Newton-Drude mathematical formulae. Single, binary and ternary systems have been examined. Thus, new data were obtained for the practical applications.

The refractive index determination of thin films by transmission Nomarski Differential Contrast (NDIC) microscopy is reported by

Holik and Taylor [30]. This technique was applied to optically isotropic solid particles and was more precise over the Becke method when used on 0.25μm thin amorphous aluminium oxide film.

3.5 Kramers-Kronig Relation

The Kramers-Kronig relation [K-K], which connects phase of the complex Fresnel equation for incidence radiation, is applied to derive the absorption data from the reflectance spectrum [31-34]. The Kramers-Kronig dispersion relation was deduced under very general conditions as follows:

$$\varepsilon_1(\omega) = 1 + \frac{2}{\pi}\int_0^{\infty} \frac{\xi\varepsilon_2(\xi)d\xi}{\xi - \omega^2} \qquad (21)$$

where ε_1 is the real part of the dielectric constant and ξ symbol refers to angular frequency of radiation of the range of interest.

The Kramers-Kronig relation is also valid for amorphous thin films and glasses as well as for crystals in the UV region. The modified Kramers-Kronig relation from transmission spectrum in the infrared region is applied [35-36] as follows:

$$n^2 = 1 + \frac{c^2\alpha^2}{16\pi^2\nu^2} + \frac{c^2\alpha(\nu_1)}{2\pi^2\nu}\ln\left(\frac{\nu_1+\nu}{\nu_1-\nu}\right) + \frac{c\alpha}{\pi^2\nu} + \frac{c}{\pi^2}\int_{\nu_0}^{\nu_1}\frac{\alpha(\nu^*)d\nu^*}{\nu_2^* - \nu^2} \qquad (22)$$

where ν is the frequency, c is the velocity of light, ν_0 is the first sub-interval and ν_1 is the last sub-interval.

The trapezoidal rule method has been used to solve the integrations of Eq. (21) and n has been computed for silica, $MgO\text{-}P_2O_5$ glasses [35-36] and for thin films [37].

3.6 Ellipsometric technique

Thin conducting films, such as In_2O_3 and SnO_2, used as electrodes of display devices must posses high transparency and electrical conductivity. Those two parameters are connected with the optical constants of the film.

The basic equation of ellipsometry parameters Ψ and Δ is:

$$\Psi = arctg\frac{\rho_p}{\rho_s} \text{ and } \Delta = \delta_p - \delta_s \qquad (23)$$

where ρ_p and ρ_s are amplitudes coefficients and δ_p and δ_s are the phase changes in reflection for parallel (p) and perpendicular (s) components of the electric field. Equation (22) expresses the dependence of these parameters on the optical constants as well as on the film thickness. Using ellipsometric technique and for film thickness (0.2-1.5)μm, the refractive index of In_2O_3 films were in the range (1.9-2.0) while for SnO_2 films varied from 1.7 to 2.0 [38].

Figure (3) depicts monogram constructed for determination of the refractive indices and thicknesses of conducting films on a glass substrate from ellipsometric parameters Ψ and Δ obtained with light at incident angle of 45° and λ=630nm.

Al-Ani and Hogarth [39] reported the optical constants of V_2O_5 thin films by ellipsometric technique. They concluded that the high absorption made it difficult to obtain reliable measurements of thickness and refractive index using a fixed angle of incidence and wavelength.

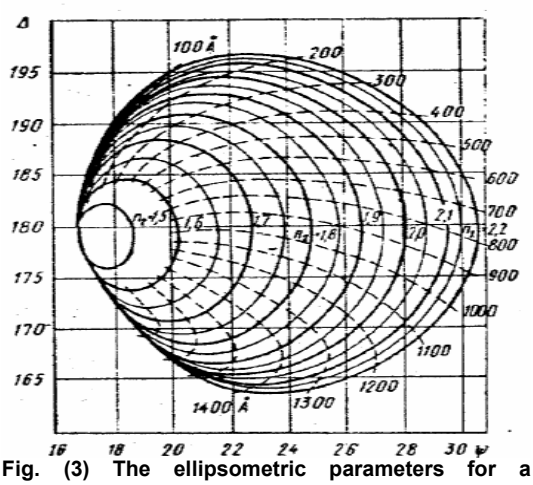

Fig. (3) The ellipsometric parameters for a conducting film on a glass substrate [38]

Irene [40] has reviewed the applications of spectroscopic ellipsometry in microelectronics with special reference to silicon technology such as oxidation, CVD, etching, interfaces and new processing techniques. It is concluded that single wavelength ellipsometry (SWE) as well as spectroscopic ellipsometry (SE) are required for optimum measurement conditions.

4. Antireflecting Thin Films

The surface reflection of light can change the index of refraction at the boundary of two materials. This has a critical effect in solar applications. Antireflection (AR) coatings vary from single layer to a combination of more than a dozen layers, having virtually zero R at one wavelength or over a range of wavelengths, respectively. The type of AR application depends on: the substrate material, the wavelength region, the required performance and the cost. For a glass-air interface R is equal to 0.04, whereas, for Ge with index 4 giving a reflection loss of about 36% and Si of index 3.5 with reflection losses of 31%. Without AR coating, it would be impossible to use these semiconductors in many applications. Hence to reduce the surface reflectance loss, an antireflecting coating layer is applied. This layer is intermediate index of refraction (n_{AR}) between the high (h)- and the

low (*l*)- index materials. The simplest approach to achieve this layer of refractive index n_{AR} and thickness *d* is obtained from:

$$n_{AR} = \sqrt{n_h n_l}\ ,\ d = \frac{\lambda}{4n_{AR}}.\frac{\Psi}{\Delta} \qquad (24)$$

where λ is the wavelength of the minimum desired reflectance of the surface

The Si_3N_4 is a candidate for a graded-index antireflecting coatings. The refractive index variation of SiO_xN_y is presented in figure (4) which can be varied between the values of SiO_2 and Si_3N_4 [41].

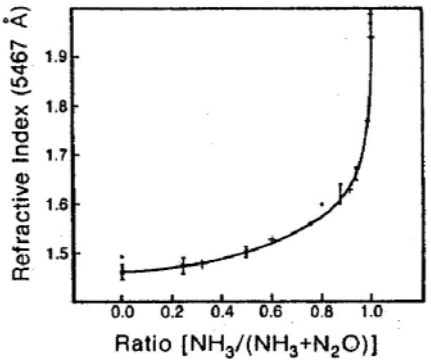

Fig. (4) The refractive index of SiO_2 and Si_3N_4 [41]

Zinc sulfide (Table 1) is used as a quarter-wave AR coating over the range 0.4-25μm. A single layer of ZnS can treat semiconductors such as Ge, Si, GaAs, InAs and InSn. Values of the refractive index of some selected thin films are also listed in table (1).

Table (1) Refractive index of some thin films [41]

Material	n_f	(μm)
Ta_2O_5	2.8	0.4
TiO_2	2.4-2.9	0.4
WO_3	2.29	0.4
ZrO_2	2.10	0.55
PbF_2	1.75	0.4
Al_2O_3	1.62	0.4
SiO_x	1.4-1.48	0.4
CeO	2.3	0.4
	2.2	2.0
SiO	1.9	
MgF_2	1.37	
ZnS	2.2	2.0
	2.15	15.0
Si	3.5	
Ge	4.0	

5. Application to a Wide Bandgap Semiconductor

The real part of the wavelength-dependent refractive index from single transmission spectrum of SrS thin film has been presented by Poelman and Smet [42].

Seven analysis methods have been applied. The same type of dispersion behavior for n_f were reproduced from these methods. The authors also presented a critical review on methods used to determine the optical constants of thin films from single transmission measurements.

These methods were:

- The Cauchy equation [43]

It is applicable to transparent materials and glasses.

$$n(\lambda) = A_n\lambda + B_n\frac{\lambda}{2} + C_n\frac{\lambda}{4} \qquad (25)$$

where λ in microns and A_n, B_n and C_n are fitting parameters.

- The Sellmeier relation [43-44].

It is also applied to transparent materials as well as semiconductors in the infrared region

$$n(\lambda) = (A_n + \frac{B_n}{\lambda} - \frac{C_n}{\lambda^2})^{1/2} \qquad (26)$$

where A_n, B_n and C_n are also fitting parameters. Although, this relation was used for completely transparent material (i, e. k=0) but it has also applied to the absorbing region.

- The Lorentz classical oscillator model [43-45].

$$n^2 - k^2 = 1 + \frac{A\lambda^2}{\lambda^2 - \lambda_0^2 + g\lambda^2/(\lambda^2 - \lambda_0^2)} \qquad (27)$$

$$2nk = \frac{Ag^{\frac{1}{2}}\lambda^3}{(\lambda^2 - \lambda_0^2)^2 + g\lambda^2} \qquad (28)$$

where λ_0 is the oscillator central wavelength and g the damping factor. The term **1** at the right-hand side of Eq. (27) represents the dielectric function at infinite wavelength. Poelman and Smet [42] have replaced it by a fitting parameter, which is the dielectric function at wavelength much smaller than measured.

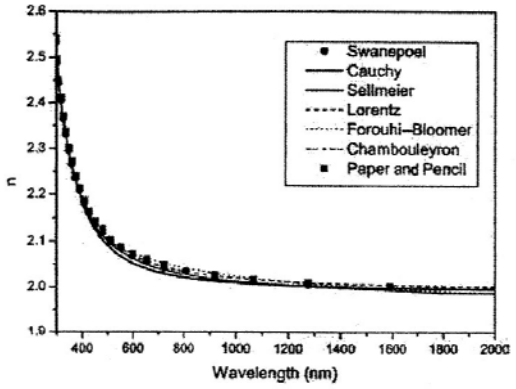

Fig. (5) The real part of the wavelength-dependent refractive index obtained from transmission spectrum [42]

The fitting parameters, A, g and λ_0 have no real physical meaning.

- Swanepoel envelope method [17].
- Forouhi-Bloomer dispersion relations [46-49]:

They are designed for crystalline semiconductors and dielectrics. Those equations were applied to energies higher than the band gap region and the sub-band gap region [50].

• Chambouleyron *et al* optimization method [51-54]

This method is to extract (n and k) from transmittance data and works with some physical constraints which valid for semiconductors and insulators in the normal dispersion region.

• The manual method of finding interference fringes. Poelman and Smet [42] have concluded that all the above methods were able to reproduce the same kind of dispersion behavior for the refractive index as in figure (5) and table (2).

Table (2) Results of different analysis methods for single transmission spectra of SrS thin film [42]

Method	Data range (nm)	Film thickness (nm)	RMS (%)
Cauchy	300 – 2000	798.3	0.71
Sellmeier	300 – 2000	796.3	0.31
Lorentz	300 – 2000	793.9	0.36
Paper and pencil	NA	792.6	NA
Forouhi – Bloomer	500 – 2000	793.0	0.38
Swanepoel	NA	794.5	NA
Chambouleyron	300 – 2000	796.6	0.22

Method	n_f(2000nm)	n_f(5000nm)
Cauchy	1.997	2.091
Sellmeier	1.995	2.101
Lorentz	2.002	2.107
Paper and pencil	1.994	2.114
Forouhi – Bloomer	1.9888	2.096
Swanepoel	1.995	2.107
Chambouleyron	1.988	2.101

RMS: deviation between experimental data and fitted results

6. Conclusions

The refractive index of thin films have shown variation with different parameters such as deposition techniques, substrate temperature, annealing temperature, degree of oxidation, mixing ratio, density, doping, hydrogen content, films thickness, non-stoichiometry, inhomogeneity, and anisotropy of the deposited films. Moreover, the variation of the refractive index on other external effects such as temperature, pressure, electric field, light intensity, exciton modulation, radiation, fatigue, etching and aging effects [55-65].

The dispersion equations mentioned above can give a good fit with the transmission spectrum over a wide range of wavelengths for many thin film materials. The dispersion curve of $n_f(\lambda)$, however, varies at different regions of the electromagnetic spectrum.

The knowledge of refractive index for thin films and the related experimental techniques is important for advanced optical and microelectronics applications. Efforts to evaluate the accuracy of these methods have been undertaken as well as some progress steps in the manufacturing area.

To conclude, it seems that the effort in the near future will be concentrated on the improvement of the available methods. But the physicists always leave the door open to the possibility of emerging novel techniques or methods, which are not necessarily complicated types.

References

[1] F. Abeles, *Compt. Rend. Acad. Sci.*, 228 (1949) 553.

[2] F. Abeles, *J. Phys. Rad.*, 11 (1950) 310-314.

[3] A. Taylor, "The preparation and properties of thin films of evaporated silicon monoxide", M.Sc. thesis, Nottingham University, U.K. (1969).

[4] P.A. Timson and C.A. Hogarth, *Thin Solid Films*, 8 (1971) 237.

[5] P.A. Timson, Ph.D. thesis, Brunel University, UK (1971).

[6] S.K.J. Al-Ani, K.I. Arshak and C.A. Hogarth, *J. Mater. Sci*., 19 (1984) 1737-48.

[7] S. Fujiwara, *J. Opt. Soc. Amer.*, 53 (1963) 880.

[8] Idem, *ibid*. 53 (1963) 1317.

[9] D.R. McKenzi et al., *SPIE*, Vol.369 Max-Born, 110-117.

[10] R.E. Denton, R.D. Campbell and S.G. Tomlin, *J. Phys. D: Appl. Phys.*, 5 (1972) 852-63.

[11] S.K.J. Al-Ani, "Studies of optical and related properties of amorphous films", Ph.D. Thesis, Brunel University, UK (1984).

[12] S.K.J. Al-Ani and C.A. Hogarth, *Int. J. Electronics*, 58 (1985) 123.

[13] S.K.J. Al-Ani and C.A. Hogarth, *phys. stat. sol. b*, 126 (1984) 293.

[14] S.K.J. Al-Ani, C.A. Hogarth and S.W.B. Abeysuria, *J. Mater. Sci.*, 20 (1985) 2541.

[15] S.K.J. Al-Ani and Y.M. Hassan, *J. Math. Phys.*, 11(1) (1989) 9-24.

[16] S.K.J. Al-Ani et al., *Int. J. Electronics*, 69(1) (1990) 87-95.

[17] R. Swanepoel, *J. Phys. E: Sci. Instrum.*, 16 (1983) 1214-22.

[18] M. McClain, A. Feldman, D. Kahaner and X. Ying, *Comput. Phys.*, 5 (1991) 45-48.

[19] D. Minkov, *Optik*, 90 (1992) 80-4.

[20] M. Di Domenico and S.H. Wemple, *J. Appl. Phys.*, 40 (1969) 720.

[21] J.C. Manifacier, J. Gasiot and J.P. Fillard, *J. Phys. E: Sci. Instrum.*, 9 (1976) 1002-4.

[22] J. Beynon, S.K.J. Al-Ani and M.M.A.G. El-Samanoudy, *J. Mater. Sci. Lett.*, 12 (1993) 308-10.

[23] D. Poelman and J. Vennik, *J. Phys. D: Appl. Phys.*, 21 (1988) 1004.

[24] F.M. Phelps and B.S. Jacobson, The Physics Teacher, March 1980, p.216.

[25] A.V. Narasimham and S.K.J. Al-Ani, *Phys. Educ.* (India) April-June (1989) 15.
[26] P. Rajagopala Rao, R.N. Chatterjee and T. Mohd and T.Mohsin, *J. Opt. Soc. Am.*, 7 (1968) 996.
[27] M.S. Mehde, S.K.J.Al-Ani and P. Rajagopala Rao, Proc. Int. AMSE Conf., Modeling and Simulation, Rio de Janerio (Brazil) Oct. 13-1, 51988, Vol.2, pp 3-13.
[28] S.K.J. Al-Ani and C.A. Hogarth, *J. Mater. Sci. Lett.*, 6 (1987) 519.
[29] S.K.J. Al-Ani and S. Al-Assawi, *J. Math. Phys.*, 13(2) (1992) 177-203.
[30] A.S. Holik and D.F. Taylor, *Microscope*, 28 (1977) 265-71.
[31] H.A. Kramers, *Atticong. Int. Fis. Comr.*, 2 (1927) 545.
[32] Idem, *Phys. Z*, 30 (1929) 521.
[33] R. Del Kronig, *J. Opt. Soc. Amer.*, 12 (1926) 547.
[34] Idem. *Phys. Rev.*, 30 (1929) 521.
[35] S.K.J. Al-Ani and Q.S. Majeed, *Iraqi J. Sci.*, 34(3) (1993) 540.
[36] S.K.J. Al-Ani, H.O. Al-Hassany, Z.T. Al-Dahan, *J. Mat. Sci.*, 30 (1995) 3720-29.
[37] S.K.J. Al-Ani, Q.S. Majeed, D.H. Al-Amiedy, *Iraqi J. Sci.*, 36(3) (1995) 945-65.
[38] G.I. Vidro, E.G. Mukhina, I.A. Morozova and E.I. Smirnova, Translated from *Zavodskaya Laboratoriya*, 43(5) (1977) 554-556.
[39] S.K.J. Al-Ani and C.A. Hogarth, *J. Mater. Sci.*, 20 (1985) 1185.
[40] E.A. Irene, *Thin Solid Films*, 233 (1993) 96-111.
[41] P.J. Call, in **"Polycrystalline and Amorphous Thin Films and Devices"**, L.L. Kazmerski, editer, Academic Press, (NY) 1980.
[42] D. Poelman and P.F. Smet, *J. Phys. D: Appl. Phys.*, 36 (2003) 1850-57.
[43] F.A. Jenkins and H.E. White, **"Fundamentals of Optics"**, (Auckland: McGraw-Hill), 1981, 482-6.
[44] B. Tatian, Appl. Opt., 23 (1984) 4477-85.
[45] E. Hecht, **"Optics"**, 2nd ed. (Reading MA: Addision-Wesley) 61.
[46] A.R. Forouhi and I. Bloomer, *Phys. Rev.* B34 (1986) 7018-26.
[47] *ibid*, B38 (1988) 1865-74.
[48] Bloomer and R. Mirsky, *Photon. Spectra*, (2002) 86-92.
[49] A.R. Forouhi and I. Bloomer, **"Handbook of Optical Constants of Solids ll"**, edited by E.D. Palik (Boston: Academic) 151-75 (1991).
[50] K. Zhang, A.R. Forouhi and I. Bloomer, *J. Vac. Sci. Technol.* A, 17 (1999) 1834-7.
[51] Chambouleyron, J.M. Martinez, A.C. Moretti and M. Mulato, *Thin Solid Films*, 317 (1998) 133-6.
[52] W.G. Birgin, I. Chambouleyron and J.M. Martinez, *J. Comput. Phys.*, 151 (1999)862-80.
[53] Chambouleyron, J.M. Martinez, A.C. Moretti, and M.Mulato, *Appl. Opt.*, 36 (1997) 8238-47.
[54] Chambouleyron, S.D. Ventura, E.G. Birgon, and J.M. Martinez, *J. Appl. Phys.*, 92 (2002) 3093-102.
[55] B.O. Seraphin, *Thin Solid Films*, 39 (1976) 87.
[56] J.N. Zemel, J.D. Jensen and R.B. Schoolar, *Phys. Rev.*, 140 (1965) A330.
[57] S.K.J. Al-Ani, C.A. Hogarth and D.N. Waters, *phys. stat. sol. b*, 123 (1984) 653.
[58] K.L. Chopra, **"Thin Film Phenomena"**, McGraw-Hill Book Comp. N.Y. (1969).
[59] N.F. Mott and E.A. Davis, **"Electronic Processes in Non-Crystalline Materials"**, 2nd ed., Clarndon Press, Oxford (1979).
[60] T.S. Moss, **"Optical Properties of Semiconductors"**, Butterworths, London (1959).
[61] J. Tauc, **"Amorphous and Liquid Semiconductors"**, Plenum Press, London (1974).
[62] D. Poelman, D. Wauters, R.L. van Meirhaeghe and F. Cardon, *Thin Solid Films*, 350 (1999) 67-71.
[63] K.K. Ng, **"Complete Guide to Semiconductor Devices"**, McGraw-Hill, Inc. (NY) (1995).
[64] J. Singh, **"Semiconductor Optoelectronics"**, McGraw-Hill, Inc., (NY) (1995).
[65] S.K.J. Al-Ani, R.H. Yousif and Th. A. Zangana, *Iraqi J. Sci.*, 40(3) (1999) 63-82.

This article was reviewed at Department of Physics, Indian Institute of Technology, Delhi, INDIA, MTA Research Institute for Technical Physics and Materials Science, Budapest, HUNGARY and School of Applied Sciences, University of Technology, Baghdad, IRAQ

SLOWING DOWN THE SPEED OF LIGHT
"Boss-Einstein Condensate for a Gas" - BEC

Written by
Intesar Al-Ramley (*professor*)
Meridex Software Corporation
Vancouver, CANADA

At the University of Colorado, a new form of matter called a Fermionic gas (Boss-Einstein condensate, BEC) has been created. It consists of almost a million atoms of Potassium cooled to a few hundred millionths of a degree above absolute zero, the coldest possible temperature - minus 273°C. The new gas follows the laws of quantum mechanics, the branch of science that describes the world of the very small in which everything, matter, energy and even space and time comes in lumps or quanta. It means that the new gas will behave in ways that can only be observed in small systems and a million atoms of Potassium are certainly very small in nature's terms. Every particle in nature can be classified as either a Fermion or a Boson. Fermions are the type of particles that make up the atom, i.e. electrons, protons and neutrons. The best known example of a boson is a photon, a particle of light. Bosons and Fermions behave in very different ways exemplified by the Pauli Exclusion Principle. In simpler terms it gives protons, neutrons and electrons a sort of identity, a space of their own that cannot be invaded by any other particle. The Pauli Exclusion Principle is the reason why atoms exist at all. Without it, Fermions would not be able to congregate in such stable structures. The Fermionic gas holds no great surprises but scientists hope that they will soon be able to cool it even further and make it condense. They say a Fermionic condensate would have very strange properties indeed.

Lene Vestergaard Hau, physicist at Harvard, managed to stop a pulse of light in mid-flight, start it up again at 0.13 miles per hour, and then make it appear in a completely different location. "It's like a little magic trick," says Hau. "Of course, in all magic tricks there's a secret." And here, the secret is a 0.1-mm lump of atoms called a Bose-Einstein condensate, cooled nearly to absolute zero (-459.67 degrees Fahrenheit) in a steel container with tiny windows. Normally - well, in a vacuum - light goes 186,282 miles per second. Things are different inside a BEC, a strange place where millions of atoms move - barely - in quantum lockstep. About a decade ago, Hau started playing with BECs - for a physicist, that means shooting lasers at them. She blew up a few. Eventually, she found that lasers of the right wavelengths could tune the optical properties of a BEC, giving Hau an almost supernatural command over any other light shined into it. Her first trick was slowing a pulse of light to a crawl - 15 mph as it traveled through the BEC. Since then, Hau has completely frozen a pulse and then released it. And recently she shot a pulse into one BEC and stopped it - turning the BEC into a hologram, a sort of matter version of the pulse. Then she transferred that matter waveform into an entirely different BEC nearby - which emitted the original light pulse. That's just freaky. Hey, Einstein may have set that initial speed limit of light, but he only theorized about BECs. "It's not breaking relativity, Hau says "but I'm sure he would have been"

To conduct such experiment, cooling will not be required, instead, confinement (with a magnetic field - passing a DC current through coils) of the gas atoms. This is followed by passing a multi beam of laser, like **X.** In the middle of **X,** the confined gas is placed. The **X** is simply made of two glass tubes fused in the middle to make the **X-shape**). With the right wavelength which matches the wavelength of these atoms (when they behave like an electromagnetic wave) we can stop most of them within the magnetic confinement - while some might escape from the confinement if they absorb the energy rather than being stopped by the laser photon momentum. Once atoms are stopped, their collection will drop dramatically because the near zero absolute temp means that all the atoms will stop from moving. So instead of using the traditional cooling techniques, laser momentum is employed to produce BEC.

Production of Ceramic-Based Composites By Self Infiltration

Nawal E. Abdul-Latif [1]
Salim A. Kako [2]

[1] *Department of Production and Minerals Engineering, University of Technology, Baghdad, Iraq*
[2] *Department of Mechanics, Technical Institute of Erbil, Erbil, Iraq*
salim_zz@yahoo.com

The aim of this work is to produce composite materials with ceramic base covered by a layer of aluminum and its alloys by means of self infiltration. Al_2O_3 powder was used after been pressed by different pressures (58MPa, 117MPa and 176MPa) in metallic mold. The sintering process has been preformed at 1200°C for two hours. After that, the porosity percentage was measured and the samples were heated to 700°C and then immersed in the molten pure aluminum and its alloys and heated to about 1000°C for half an hour .Then the samples were cooled to 650°C and examined by an optical microscope and the scanning electron microscope. Moreover, the x-ray diffraction for the samples has been employed to define the structure of the resulting composite .The testing results reveal that the immersing process can be successfully done in Al-Mg alloy to obtain composite material of ceramic base with metal layers.

Keywords: *Composites, Ceramic-metal bonding, Fused deposition*
Received 2 April 2006, Revised 4 July 2007, Accepted 25 March 2008

1. Introduction

Recently, the interest in production of composites metals and ceramics is increased. This interest is aiming to enhance several properties such as strength, stiffness, wear resistance and high thermal standing in order these composites being used instead of many other conventional alloys [1-2]. Several methods were considered to produce such composites such as powder technology [3], alloying [4], thermal and chemical deposition [5]. As the need for ceramics used in various engineering applications, from cutting tools to the internal combustion engines of space crafts, is improved, the concentration on enhancing and improving the properties of such composites is increased by producing ceramic-matrix composites [7]. Nowadays, the most important uses of these composites is focused on structure materials, electronic devices [8-9] , magnetic and optical applications, as well as thermal management applications such as electronic packaging [10].

All above applications requires the composite to have high thermal conductivity and low thermal expansion coefficient in addition to high toughness. Hence, the required ceramic- matrix composites are produced as plates or layers bonded by solid-state diffusion or resin bonding method [11]. The composites produced by solid-state diffusion bonding of ceramics and metals, like gold and platinum, have good mechanical properties. However, this bonding method is limited because it produces thin bonding surfaces, requires pre-bonding polishing and grinding processes [12], in addition to its high production cost. Therefore, the researches are focused on finding other methods such as immersing and liquid-state deposition to produce such composites. This work is an attempt in this field.

2. Experiment

High- purity α-Al_2O_3 powder was used and the grain sizes and volumetric distribution were measured by LA 22-6 granometer. The grain sizes were (1-11) microns and table (1) explains the chemical composition of Al_2O_3 powder used. Pure aluminum, aluminum with 2.26%Mg and aluminum with 5.6% Mg, were used as molten alloys and tables (2-4) explain the results of chemical analysis.

After the volumetric analysis of alumina powder, the ceramics were formed by a hydraulic press of 1.4 mm diameter at pressures of 58MPa, 117MPa and 176MPa for 30 seconds. After with, the samples were placed on alumina substrates and the elementary sintering was employed using a Carbolite electrical furnace at 1200°C for 2 hours at 6°C/min heating rate to ensure not forming cracks and voids or causing delamination. The samples were then cooled room temperature. In order to choose the

optimum samples, the macroscopic test was performed using a magnifying lens to choose the samples whose surfaces are free from the cracks and voids.

Table (1) The chemical composition of Al_2O_3 powder

Elements	Concentration (ppm)
Purity	99.97
Na	22
Si	34
Fe	18
Ca	15
Mg	8
Ti	< 5
Ga	< 5

Table (2) The chemical composition of pure aluminum

Cu %	Fe %	Mn %	Si %	Mg %	Al %
0.3062	0.467	0.028	0.1153	0.1063	98.9772

Table (3) The chemical composition of 2.26% Mg-Al alloy

Si %	Fe %	Cu %	Mn %	Mg %	Zn %
0.257	0.215	0.04	0.0042	2.26	0.0025
Ti %	Cr %	Pb %	Ni %	Na %	Al %
0.0041	0.3025	0.0004	0.00095	0.00095	96.919

Table (4) The chemical composition of 5.9%Mg-Al alloy

Cu %	Fe %	Mn %	Zn %	Mg %	Si %
0.1324	0.2419	0.1132	0.3355	5.920	0.8934
Al %					
Rem					

As the apparent porosity is defined as the ratio of the open pores to the total volume [14], the Archimedes principle was considered to determine this porosity as follows [15]. The sample was weighted using a 0.0001gm accurate balance from Metler after being dried in a Heraeus furnace at 120°C for 5 hours. This weight is denoted by ***D***. The sample was weighted as being immersed in boiled water for 24 hours. This weight is denoted by ***I***. The samples was dried with a cloth then weighted. This weight is denoted by ***S***. Then the apparent porosity (***A.P.*** %) is determined by:

$$A.P(\%) = \frac{(S-D)}{(S-I)} \times 100\% \qquad (1)$$

Ceramic samples were placed in a metallic basket, as shown in figure (1), then in a melting pot to be heated to 700°C. As well, the aluminum and its alloys were placed inside Carbolite furnace and melted at 700°C. Ceramic samples were divided into three groups. Each group was immersed in different molten (pure Al, Al with 2.26% Mg, Al with 5.9% Mg) then returned to the furnace to be heated to 1000°C. Figure (2) shows the flow chart of the experimental steps of this work. Samples were grinded in wet environment using Sic grinding paper of different grades (220, 500, 600 and 1000). Then 10%HF acid was used for etching process. The SEM and XRD were performed to introduce the microstructure and formed phases in the produced samples, respectively.

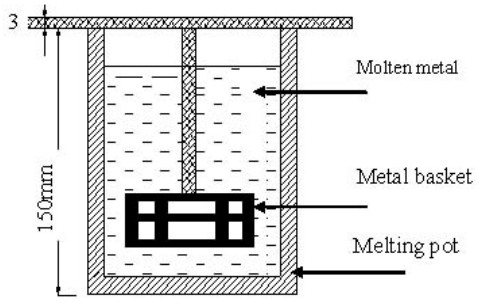

Fig. (1) The melting pot used in immersing process

3. Results and Discussion

As ceramic samples being heated inside the molten to 1000°C, the metallic layer was not thick enough on the ceramic surfaces. This layer was then foliated and dislocated from the surface in addition to large cracks on the ceramic surface, as shown in figure (3).

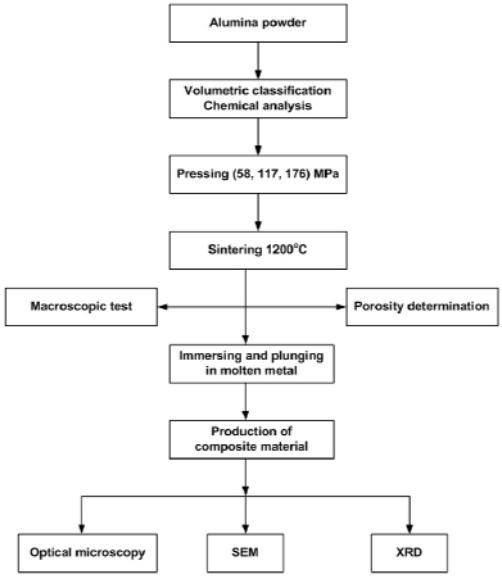

Fig. (2) The flow chart of the experimental work

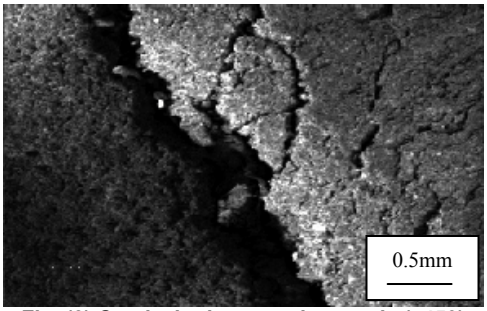

Fig. (3) Cracks in the ceramic sample (x450)

Also, as the ceramic samples were heated to 1000°C and kept at this temperature for a certain period (30 min) then cooled to 650°C, thick metallic layer was deposited on the ceramic surface as shown in figure (4).

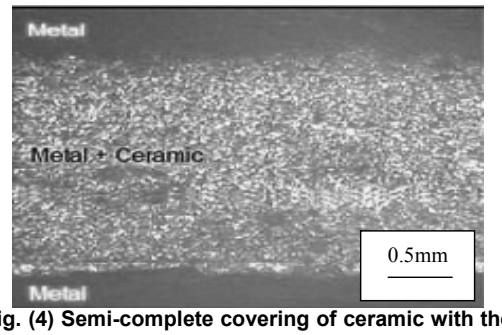

Fig. (4) Semi-complete covering of ceramic with the metal molten (x250)

As well, distinguished regions were formed between the ceramic surface and the metallic layer and partial infiltration of the metal was occurred in the regions near the ceramic surface as shown in figure (5).

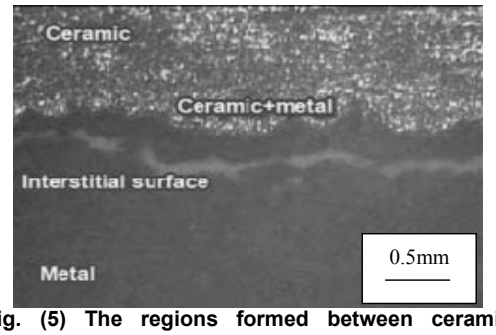

Fig. (5) The regions formed between ceramic surface and the deposited metal (x250)

Figure (6) shows the relation between pressing pressure and the percentage porosity of the ceramic sample after sintering. It is observed that the porosity decreases with increasing pressure. This percentage porosity was determined to be 25%, 30% and 38% at pressures of 176MPa, 117MPa and 58MPa, respectively, at 1200°C temperature.

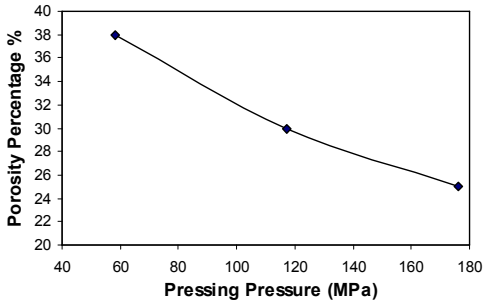

Fig. (6) The relation between porosity percentage and pressing pressure

Figure (7) shows the SEM results of the ceramic samples at different pressing pressures and sintering temperature of 1200°C. Figure (8) explains the effect of immersing process on the porosity of the ceramic samples as an additional sintering for the Al_2O_3 powder is occurred in the regions near ceramic-metal interface. Using immersing method and according to the optical and SEM measurements, ceramic- based composites surrounded by metallic layers from one or two sides were obtained with presence of regions containing metal-ceramic structure between the ceramic surface and the metallic layer, and the thickness of such regions is determined by the process variables.

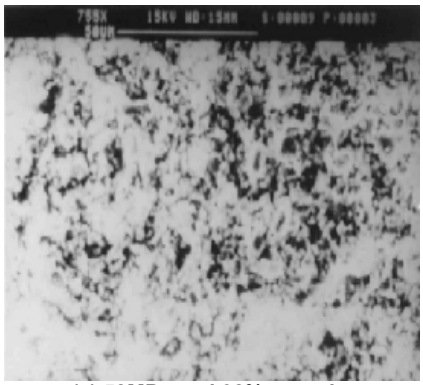

(a) 58MPa and 38% porosity

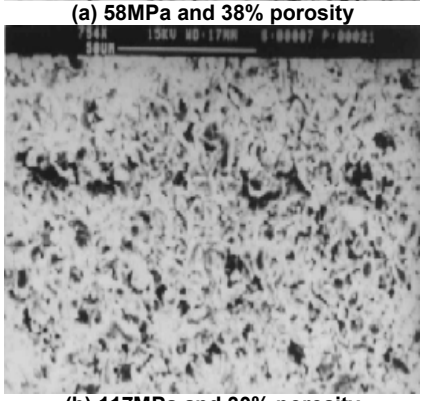

(b) 117MPa and 30% porosity

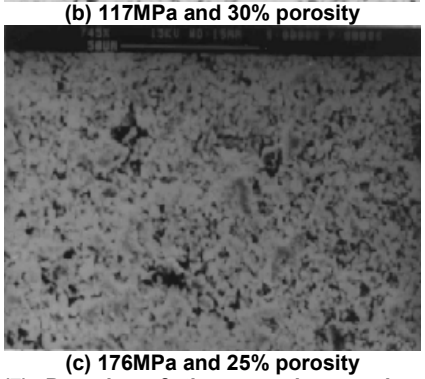

(c) 176MPa and 25% porosity

Fig. (7) Porosity of the ceramic samples after sintering at 1200°C

Due to SEM results, the high percentage porosity of the ceramic sample lead to crash or fracture in the ceramic surface when being immersed in the molten as well as increased the chance or probability for the molten to fill most of the pores inside ceramic sample normally due to the capillary properties [16]. Whereas

decreasing the porosity lead to decrease the infiltration as well as the thickness of the layer formed from infiltration of the molten within the ceramic structure. Also, the volumetric ratio of the metal is decreased with respect to that of alumina grains in this layer as shown in figure (9). In case of ceramic samples immersed in the molten of pure aluminum, thin layer of aluminum was deposited on the ceramic surface but with weak bonding as shown in figure (10). The XRD showed only alumina phases which represent the ceramic structure. Absence of phases resulted from Al-Al_2O_3 reactions caused to decrease metal-ceramic bonding and hence dislocating layers from each other. This may be attributed to the presence of internal stresses due to the difference in expansion coefficients of aluminum and alumina [17].

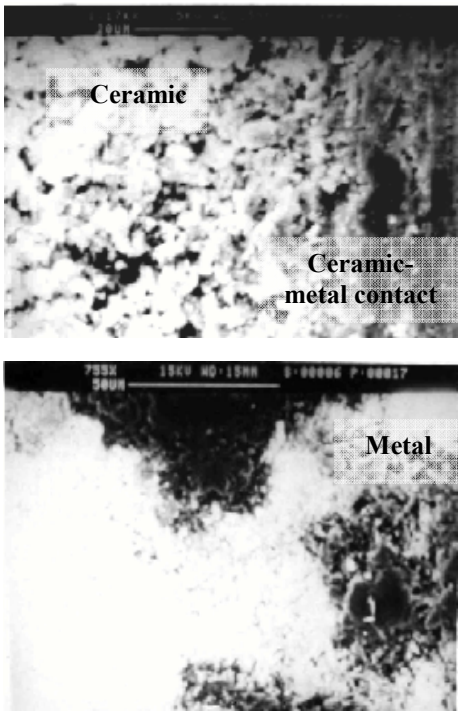

Fig. (8) The sintering of alumina during immersing in the molten metal

The SEM results of the ceramic samples immersed in Al-Mg molten showed distinguished layers; layer of the metal deposited on the ceramic surface and the other of metal-ceramic structure. The latter can be considered as a composite containing of alumina particles immersed in the molten metal filling the pores in the ceramic structure. A third distinguished layer is the base ceramic. Figure (11) indicates these layers whose thickness varied with the varying porosity of the ceramic sample. Also, increasing the amount of Mg in the Al-Mg molten leads to increase the thickness of composite layer resulted from infiltration of metal in the ceramic structure, as shown in figure (12).

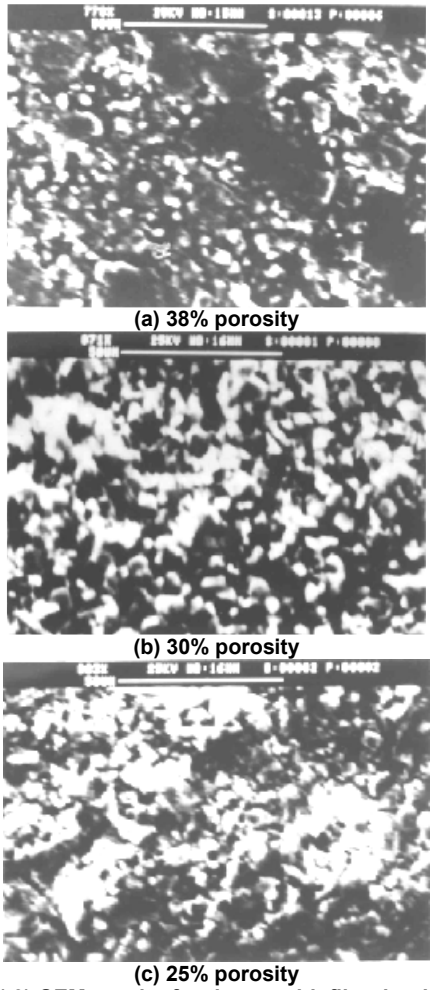

(a) 38% porosity

(b) 30% porosity

(c) 25% porosity

Fig. (9) SEM results for the metal infiltration in the ceramic sample

The presence of Mg caused to change the surface properties of alumina throughout changing the surface stress and decreasing wetting angle between ceramic grains and metal and hence increasing metal-ceramic bonding [18]. It also increases the chance of reaction and formation of spinal phases among alumina grains that improve bonding with metal [19]. Increasing the thickness of this layer leads to decrease the resulted internal stresses and hence the possibility of dislocating the metal layer from the ceramic surface.

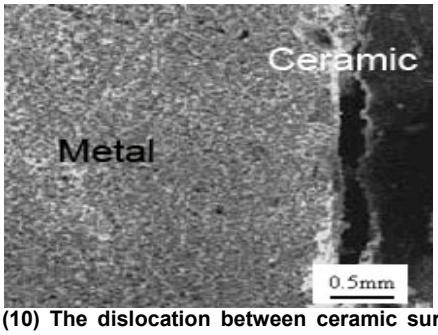

Fig. (10) The dislocation between ceramic surface and metallic layer (x200)

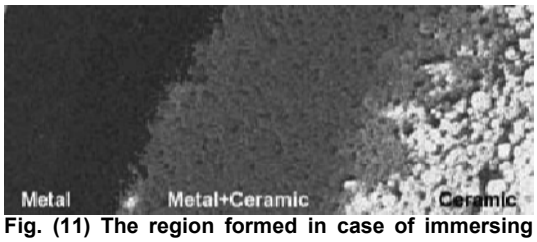

Fig. (11) The region formed in case of immersing ceramic sample in Mg-Al molten (x450)

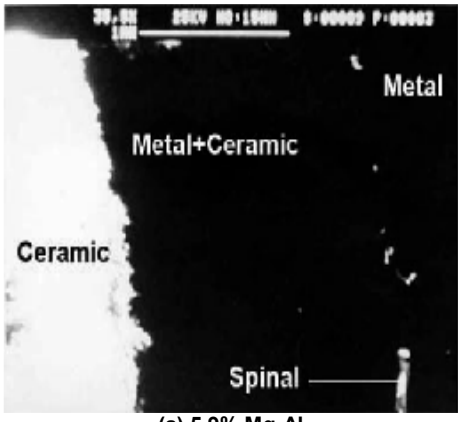

(a) 5.9% Mg-Al

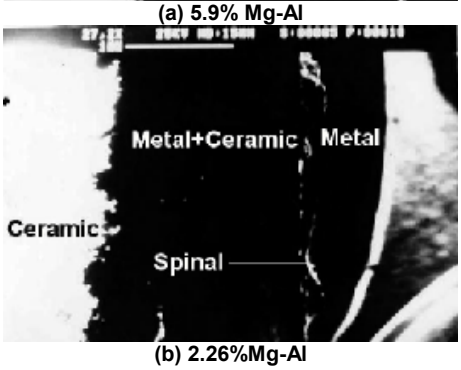

(b) 2.26%Mg-Al

Fig. (12) Effect of the molten on the spinal layer thickness formed in the 30% porosity ceramic sample

According to the XRD results shown in figure (13), three phases were distinguished; they are a-Al_2O_3 of the ceramic substrate, Al and spinal including $MgAl_2O_4$ and $MgOAl_2O_3$. These results confirmed the occurrence of a reaction between alumina particles and metallic molten containing Mg leading to spinal phase formation within the interstitial surfaces. Hence, the bonding between ceramic and metallic phases is increased and the probability of spinal phase formation is accordingly increased with increasing Mg amount in the alloy due to increasing wetting of alumina by the molten. This increases alumina-metal contact and hence their reaction and spinal phase formation. The formation of these phases on the interstitial surfaces increases the chance of the employed method to produce composites from ceramic and metal as bonded layers with good properties.

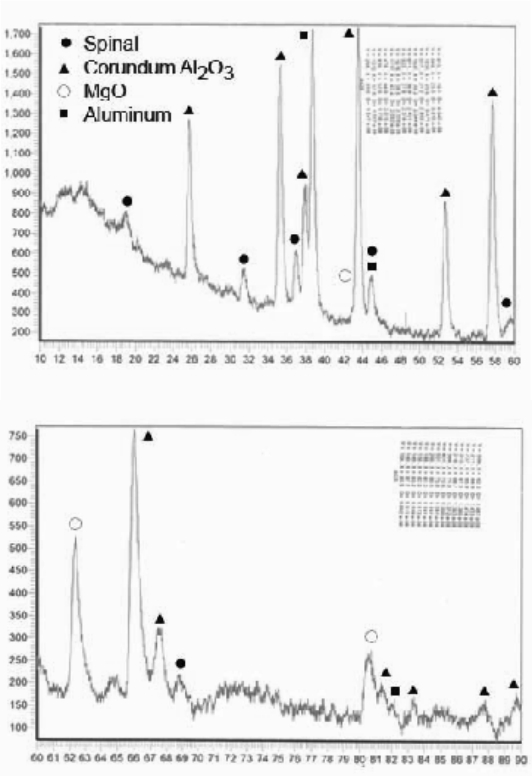

Fig. (13) The XRD pattern of ceramic sample immersed in 2.26%Mg - Al molten

4. Conclusion

According to the obtained results, we can produce ceramic-metal composites by plunging ceramic samples in metallic molten. High porosity of the ceramic sample caused fracture or crash in the ceramic surface as being plunged in the molten metal and hence decreased ceramic-metal bonding. No bonding was occurred when the ceramic sample plunged in the pure molten aluminum. Layers of the metal deposited on the ceramic surface were formed as the ceramic sample plunged in molten Mg-Al.

References

[1] M. Kutz, **"Mechanical Engineers Handbook"**, John-Wiley & Sons, 1998, pp.131-132.

[2] A. Chaklader and K.R. Linger, *Composites*, October 1976, pp.239-243.

[3] C.W. Harrigan, *Mater. Sci. Eng.* Vol.A244, 1998, pp.75-79.

[4] J. Rocher et al., *J. Mater. Sci.*, Vol.24, 1989, pp. 2697-2703.

[5] J.H. Je and J. Lee, *J. Mater. Sci.*, Vol.20, 1985, pp.643-647.

[6] S.T. Bulujan, *Ceramic Bulletin*, Vol.68, No.2, pp.387-393, 1989.

[7] M.H. Lewis, **"Ceramic to be joined 10 years from now"**, Designing interfaces, Elsevier Applied Science, 1988, pp.271-273.

[8] M. Ruhle and W. Mader, **"Structure and chemistry of metal/ceramic"**, Designing

interfaces, Elsevier Applied Science, 1989, pp.145-163.
[9] J. Requena et al., *J. Amer. Ceram. Soc.*, Vol.72, No.8, 1989, pp.1511-1513.
[10] Y.L. Shen, *Mater. Sci. Eng.*, Vol. A252, 1998, pp. 269-275.
[11] J.D. Cawley, *Ceramic Bulletin*, Vo1.68, No.9, 1989, pp.1619-1622.
[12] B.J. Dalgleish et al., *Acta Metallurg.*, Vo1.37, No.7, 1989, pp.1923-1931.
[13] J.S. Khashan, M.Sc. Thesis, University of Technology, Baghdad, 2002.
[14] W. Ryan and C. Radford, **"White Wares: Production, Testing and Quality and Quality Control"**, Pergamon Press, 1987, pp.224-232.
[15] ASTM: C373, 1987.
[16] N.J. Shaw, "Densification and coarsing during solid state sintering of ceramics", P.M.I ., Vol.21, No.3, 1989, pp.6-20.
[17] M.V. Kevorkijan, *Proceedings of the American Society for Composites*, Technomic Publishing Co. Inc., 1997, pp.971-972.
[18] G. Martin, **"Encyclopedia of composite materials and components"**, John-Wiley & Sons, 1983, pp.588-602.
[19] N.A. Travitzky and A. Shlayen, *Mater. Sci. Eng.*, Vol. A244, 1998, pp. 154-160.

This article was reviewed at Department of Ceramic and Materials Engineering, McLaren Center for Ceramic Research, USA, Materials Science Division, Department of Materials Science and Engineering, Nagasaki University, JAPAN and School of Applied Sciences, University of Technology, Baghdad, IRAQ

Optical and Electrical Properties of ZnO Thin Films Prepared by Spray Pyrolysis Technique

Ali J. Mohammad[1]
Ali M. Mousa[2]
Kadhim H. Hussain[1]

1 *Department of Physics, College of Science, Almustansiriyah University, Baghdad, Iraq*
spiritjabir@yahoo.com
2 *School of Applied Sciences, University of Technology, Baghdad, Iraq*

In this work, ZnO thin films were prepared using spray paralysis technique at different molarities of aqueous zinc chloride solution. This study focused on the effect of morality on the optical and electrical properties, therefore, many samples were produced to explore and determine the optimum characteristics of the prepared samples. These properties include the optical properties such as transmittance, bandgap energy, skin depth, carrier concentration, photoconductivity, absorption edge shift, optical constants such as absorption coefficient and extinction coefficient, and electrical properties such as I-V characteristics, electrical conductivity and resistivity under dark or illumination conditions.

Keywords: *ZnO films, Spray pyrolysis, TCO films, optical properties*
Received 20 November 2006, Revised 18 March 2008, Accepted 25 March 2008

1. Introduction

Transparent conducting oxide (TCO) films have found extensive applications in optoelectronic devices [1] (for example, solar cells [2], liquid crystal displays, heat mirrors and multiplayer photo-thermal conversion system [3]). Zinc oxide has attracted attention as a transparent conducting oxide because of its (i) large bandgap (≈3.3eV) [4], (ii) high conductivity, (iii) ease in doping, (iv) chemical stability in hydrogen plasma [5], (v) thermal stability when doped with III group elements [6], and (vi) abundance in nature and non-toxicity. Zinc oxide can be applied in UV-emitting diodes, piezoelectric devices, electron-field emitters, heterogeneous catalyst for methanol synthesis and short wavelength electrooptic devices [7]. In addition, ZnO thin films also find application as gas sensors [6], because of their high electrical resistivity. The optoelectronic properties of ZnO thin films depend on the deposition and post-deposition treatment conditions as these properties change significantly with (i) the nature of chosen doping element, (ii) the adsorption of oxygen that takes place during film deposition, (iii) film deposition temperature and (iv) desorption during annealing treatment in a reducing atmosphere [8].

Several deposition techniques are used to grow aluminium-doped zinc oxide (AZO) thin films. These include chemical vapor deposition (CVD) [8-9], magnetron sputtering [10-13], spray pyrolysis [14-15], and pulsed laser deposition (PLD) [16-17]. In comparison with other techniques, PLD has many advantages such as (i) the composition of the films grown by PLD is quite close to that of the target, (ii) the surface of the films is very smooth, (iii) good quality films can be deposited at room temperature due to high kinetic energies (>1 eV) of atoms and ionized species in the laser-produced plasma [18].

Spray pyrolysis is a useful alternative to the traditional methods for obtaining ZnO thin films, because of its simplicity, low cost and minimal waste production. The spray pyrolysis process allows the coating of large surface and it is easy to include in an industrial production line. This technique is also compatible with mass production systems. With spray pyrolysis, the solution is sprayed directly onto the substrate. A stream of gas, e.g., compressed air, can be used to help the atomization of solution through the nozzle. The properties of the deposited material can be varied and controlled by proper optimization of spraying conditions. In spray pyrolysis technique, low resistive ZnO films are obtained either by post-deposition heat treatment in vacuum or by hydrogen atmosphere or by adding donor impurities such as aluminum or indium [19-20].

2. Experiment

ZnO films were prepared on borosilicate glass substrates by a homemade spray pyrolysis system. The different molarities of spray solution (0.3, 0.5, 0.6, 0.7)M of zinc chloride ($ZnCl_2.2H_2O$) were dissolved in distilled water

and the solution was carried by the compressed air as a carrier gas then fed into a spray nozzle. The flow rate of solution was 10ml/min flows from a 0.5mm-diameter nozzle at a distance of 25cm to the substrate. The substrate temperature was kept constant at (350°C). The single spraying time was (5sec) with different number of sprays. Table (1) explains the preparation conditions of the four samples.

The film thickness was measured by weight difference method assuming the density of the deposited film to be same as that of the bulk, as following

$$t = \frac{\Delta m}{\rho A}$$

where Δm is the mass difference before and after deposition, ρ is the density, and A is the film surface area.

The ohmic contacts were made of low-resistivity aluminum electrodes produced by thermal evaporation on the surface of high-resistivity ZnO thin films with spacing area of ($0.5cm^2$).

Table (1) preparation conditions of the samples prepared in this work

Sample	Molarity (M)	Film thickness (nm)
#1	0.3	765.1
#2	0.5	939
#3	0.6	1026
#4	0.7	1210

A double-beam spectrophotometer (CECIL CE 7200 Aquarius) operating in the UV/VIS regions was used for the optical transmittance measurements. The optical transmittance at normal incidence was recorded in the wavelength range of (375-900) nm.

Electrical characterization of ZnO films, including I-V characteristics in dark and under illumination, were carried out. Measurements under illumination were performed using a halogen lamp $(24V, 250W)_{max}$, a power supply (FARNELL E350) (350V, 100mA) and a digital multimeter (Tektronix CDM 250). The exposure time was 30s and the electrode spacing was 1cm while the distance between the lamp and the sample was 20cm.

3. Results and Discussion

Transmittance is explained in Fig. (1) as a function of the incident wavelength for all ZnO thin film samples. The optical properties of the spray pyrolysed ZnO films are similar to those produced by using other methods.

It is clear that the transmittance is continuously increasing with increasing wavelength to reach about 55% at 900nm. Also, the transmittance is inversely proportional to the molarity, which is in accordance with the well-known Beer's law. It is right that thickness is an important parameter in such relation, but the concentration has much effect on the transmission. The decrease in transmittance at higher molarities may be due to the increase in thickness of the films.

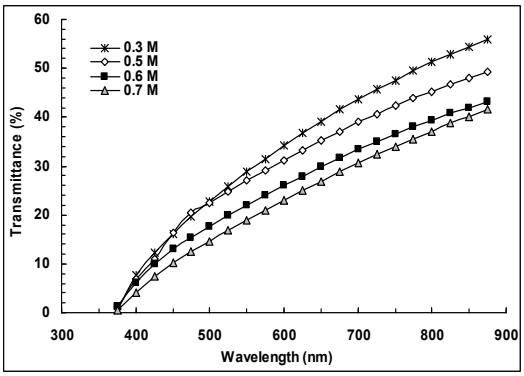

Fig. (1) Transmittance of the prepared ZnO thin films versus incident wavelength

Consequently, the absorption coefficient (α) is determined by the following relation:

$$\alpha = -\frac{LnT}{t} \qquad (1)$$

Fig. (2) shows the calculated absorption coefficient rapidly decreasing with the increasing incident wavelength (λ) and all samples seem to have close values for α at NIR wavelengths. This is a characteristic feature for all TCO thin films that they found many applications in MIR optoelectronic devices. It is worth to mention that the absorption coefficient is necessarily determined by overall preparation conditions.

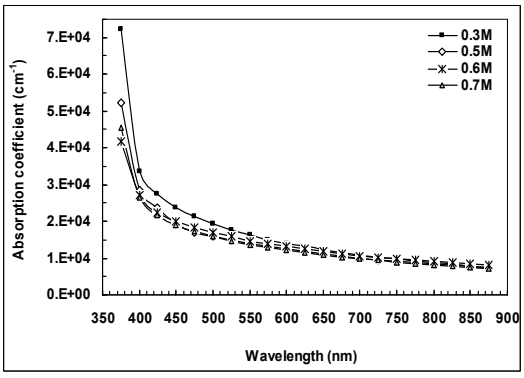

Fig. (2) Absorption coefficient of prepared samples versus incident wavelength

The extinction coefficient (k_{ex}) is determined by the following relation:

$$k_{ex} = \frac{\alpha\lambda}{4\pi} \qquad (2)$$

So, its behavior with wavelength shown in Fig. (3) is the same as for the absorption coefficient (α). The effect of the extinction coefficient on the refractive index, and hence

reflectance, is relatively higher than that of the real refractive index.

In the photonic processes, light incident on a sample is absorbed in a length characterized by the optical skin depth (ζ), which is given by:

$$\zeta = \frac{\lambda}{2\pi k_{ex}} \qquad (3)$$

In this optical skin depth, electrons can be excited to ionization states and are eventually emitted. The behaviour of the skin depth with the incident wavelength is just a reciprocal to that of the absorption coefficient multiplied by 2. Fig. (4) shows the variation of skin depth (ζ) with the incident wavelength.

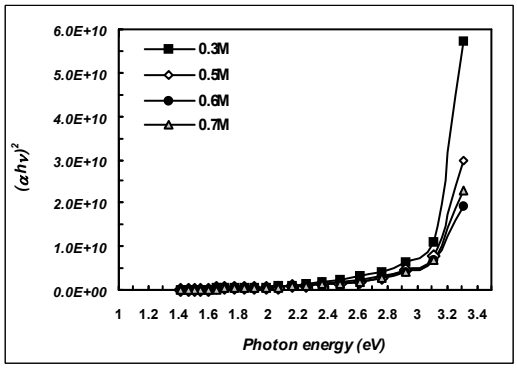

Fig. (3) The $(\alpha h\nu)^2$-$h\nu$ relation to determine type and value of energy bandgap of the prepared samples

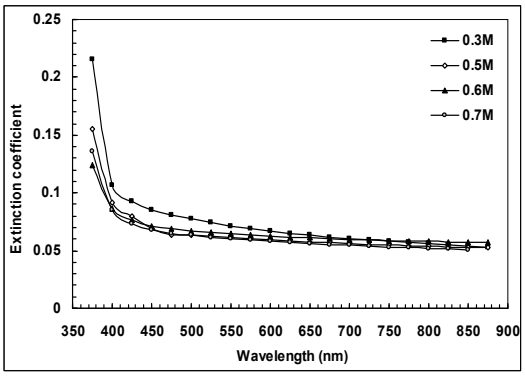

Fig. (4) Extinction coefficient of prepared samples versus incident wavelength

In order to determine the type of energy gap in the prepared ZnO samples, $(\alpha h\nu)^n$ was plotted versus the incident photon energy, and the linear bahvior was obtained from the relation between $(\alpha h\nu)^2$ and $h\nu$ as shown in Fig. (5). It is explained that the prepared ZnO sample has a direct bandgap and the allowed absorption processes are the dominant. Extrapolation of the linear portion of the plot to the energy axis yielded the bandgap value between 3-3.1eV, which is narrower than the reported value (3.37eV) by others [7, 19-20, 22-25]. The discrepancy between the obtained and reported values is attributed to the preparation conditions of the samples as well as electron-electron and electron-impurity scattering.

In all semiconductors, both optical and electrical properties are dependent of carrier concentration as these materials are mainly classified from conductors and insulators due to their properties. So, the relation between carrier concentration and incident photon energy for all ZnO thin film samples is shown in Fig. (6).

As the carrier concentration (N_e) is directly proportional to the plasma frequency (ω_p), which is in turn directly proportional to the absorption coefficient (α), as follows [26]:

$$N_e = \frac{m_e \varepsilon_0}{e^2}\omega_p = \frac{m_e \varepsilon_0}{e^2}\left(\frac{\alpha c}{2}\right) \qquad (4)$$

where m_e and e are electron mass and charge, respectively, and ε_0 is the vacuum permittivity. Sample (#1) seems to have the maximum carrier concentration while the three other samples (#2, #3 and #4) have convergent values.

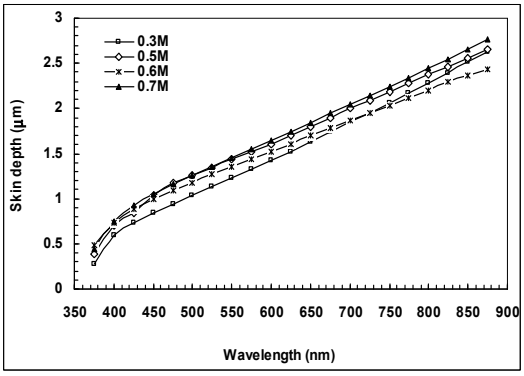

Fig. (5) the calculate skin depth of prepared samples versus incident wavelength

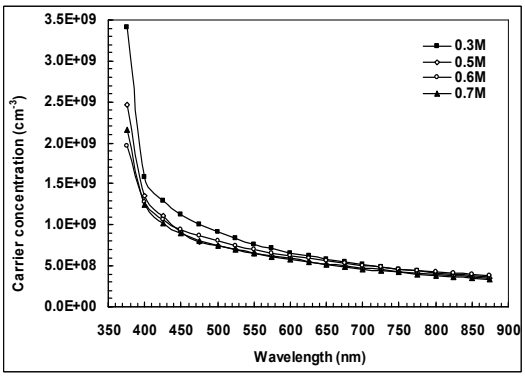

Fig. (6) The calculated carrier concentration of prepared samples versus incident wavelength

The relation between carrier concentration and incident photon energy, shown in Fig. (6), is used to determine the absorption edge (ΔE) according to Burstein-Moss model as:

$$\Delta E^{BM} = \left(\frac{\hbar^2}{2m^*_{vc}e}\right)\left(3\pi^2\right)^{\frac{2}{3}} N^{\frac{2}{3}} \qquad (eV) \quad (5)$$

where the reduced effective mass is given by

$$\frac{1}{m_{vc}^*} = \frac{1}{m_v^*} + \frac{1}{m_c^*} \quad (6)$$

According to Wolff model,

$$\Delta E^{Ex} = -\left(\frac{e}{2\pi\varepsilon_0\varepsilon_r}\right)\left(\frac{3}{\pi}\right)^{\frac{1}{3}} N^{\frac{1}{3}} \quad (eV) \quad (7)$$

In highly n-doped semiconductor, the conduction band is shifted downwards by ΔE^{Ex}. The shift in absorption edge can be determined by:

$$\Delta E = E_g - E_{g0} = \Delta E^{BM} - \Delta E^{Ex} \quad (8)$$

E_{g0} is the bandgap of intrinsic semiconductor. The conduction band shift is about 0.25eV.

Accordingly, as the photoconductivity (σ_o) is a dynamic property of semiconductor, it is related to the carrier concentration (N_e) as:

$$\sigma_o = \frac{2k_{ex}e^2}{m_e} N_e \quad (9)$$

It is shown in Fig. (7) that the photoconductivity varies with incident photon energy just same as the carrier concentration. So, sample (#1) has the maximum conductivity compared to the other three samples.

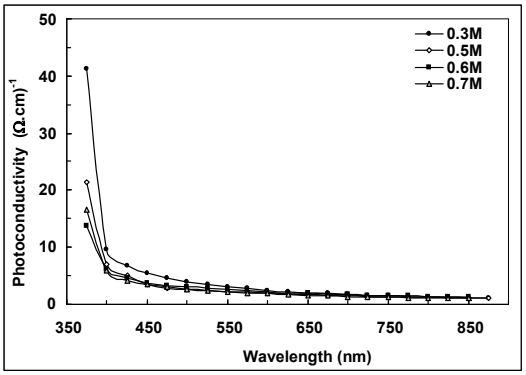

Fig. (7) The calculated photoconductivity of prepared samples versus incident wavelength

In order to determine the type of scattering contained in the ZnO structure, a relation between Ln(α)-Ln(λ) is plotted, as shown in Fig. (8), to deduce the the slope (p) as [27]:

$$p = \frac{Ln(\alpha)}{Ln(\lambda)} \quad (10)$$

As the maximum value of p is about 1.887, then the scattering is attributed to the acoustic phonons.

Fig. (9) shows the I-V characteristics of ZnO films in dark while Fig. (10) shows the variation of electrical conductivity under illumination with bias voltage for all samples.

The resistivity decreases as the current increases with increasing molarity especially at higher molarities leading to decreasing the grain boundaries.Hence, the Schottky barrier is decreased and more carriers will cross it causing the current to grow up.

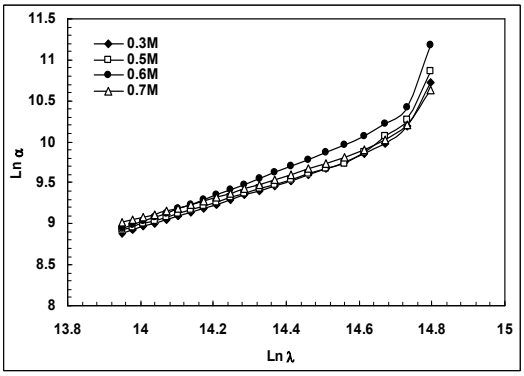

Fig. (8) The Ln(α)-Ln(λ) relation to deduce the value of p-parameter

Due to the I-V characteristics of sample (#3), the current was increased by a factor of 3 as the bias voltage increased by a factor of 2. This explains good rectification characteristics for this sample when being compared to other three ones. Also, it had the maximum conductivity exceeding the value of $0.45\Omega^{-1}.cm^{-1}$ when compared to the three other samples. The preparation conditions of sample (#3) seem to be the optimum to obtain good electrical characteristics.

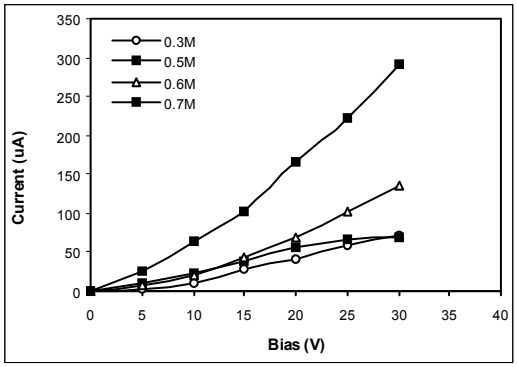

Fig. (9) The I-V characteristics of prepared samples in dark

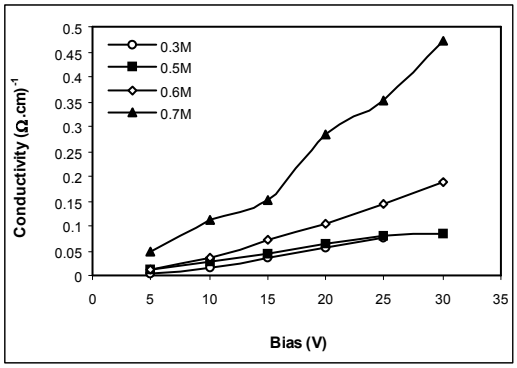

Fig. (10) The electrical conductivity of prepared samples versus biasing voltage

4. Conclusion

From the obtained results in this work, the ZnO thin films prepared by spray pyrolysis technique showed good optical and electrical characteristics. The transmittance of the prepared films was rapidly increased as the incident wavelengths varied from UV to NIR regions. For the ZnO thin films prepared at 0.3 molarity, 350°C substrate temperature, 25cm from the spray nozzle to the substrate, 2 drop/sec flow rate and 25 sprays, the thickness was 765nm and they showed the best properties. Their optical parameters were $7.21x10^{4}cm^{-1}$ absorption coefficient, 0.215 extinction coefficient, 277nm minimum skin depth, $3.4x10^{9}cm^{-3}$ carrier concentration, $41F/cm^{2}.s$ photoconductivity, direct bandgap and the allowed absorption processes are the dominant. On the other hand, the ZnO thin films prepared at 0.6 molarity, produced 1.026um thickness and explained the best electrical characteristics.

References

[1] Dower, A.L. and Joshi, J.C. *J. Mater. Sci.,* 1984, 19, 1.

[2] Ronovich, J.A., Golmoya D. and Bube, R.H. *J. Appl. Phys.,* 1980, 51, 4260.

[3] Chopra, K.L., Major S. and Panday, D.K. *Thin Solid Films,* 1983, 102, 1.

[4] Malik, A., Seco, A., Nunes, R. Vieira, M., Fortunato, E. and Martins, R. *Flat Panel Display Materials III, MRS Proc*., Materials Research Society, Vol. 471, p. 47.

[5] Shanti, E., Banerjee A., and Chopra, K.L. *Thin Solid Films*, 1983, 108, 333.

[6] Tansley, T.L., Neely, D.F. and Faley, C.F. *Thin Solid Films*, 1984, 117, 19.

[7] Lee, J., Nam, S.C. and Tak, Y., *Korean J. Chem. Eng.*, 2005, 22(1), 161-164.

[8] Nunes, P. et al., *Vacuum*, 1999, 52, 45.

[9] Hu, J. and Gordon, R.G., *J. Appl. Phys.*, 1992, 71, 880.

[10] Oda, S. et al., Jap. *J. Phys.* 1, 1985, 24, 1607.

[11] Minami, T., Oohashi, K., Takata, S. and Mouri, T., *Thin Solid Films*, 1990, 193/194, 721.

[12] Minami, T., Sato, H., Natnto, H. and Takata, S., *Jap. J. Appl. Phys.* 2, 1985, 24, L781.

[13] Igasaki, Y. and Saito, H., *J. Appl. Phys.*, 1991, 70, 3613.

[14] Aktaruzzaman, A., Sharma, G.L. and Malhotra, L.K., *Thin Solid Films*, 1991, 198, 67.

[15] Goyal, D., Solanki, P., Maranthe, B., Takwale, M. and Bhide, V., *Jap. J. Appl. Phys.* 1, 1992, 31, 361.

[16] Suzuki, A., Matsushita, T., Wada, N., Sakamoto, Y. and Okuda, M., *Jap. J. Appl. Phys.* 2, 1996, 35, L56.

[17] Hiramatsu, M., Imaeda, K. and Horio, N., M., *J. Vac. Sci. Technol.* A, 1998, 16, 669.

[18] Chrisey, B.D. and Hubler, G.K., "Pulsed Laser Deposition of Thin Films", Wiley, 1994.

[19] Benny, J., Manoj, P.K. and Vaidyan, V.K., "Studies on preparation and characterization of indium doped zinc oxide films by chemical spray deposition", *Bull. Mater. Sci.*, 2005, 28(5), 487-493.

[20] Gümüş, C., Ozkendir, O.M., Kavak, H. and Ufuktepe, Y., "Structural and optical properties of zinc oxide thin films prepared by spray pyrolysis method", *J. Optoelect. Adv. Mater.*, 2006, 8(1), 299-303.

[21] Kasap, S.O., Solved problems in optical properties of materials, private communications, 2001.

[22] Golego, N. and Studenikin, S., *J. Electrochem. Soc.*, 2000, 147(4) 1592-1594.

[23] Tang, X., Clauzonnier, A., Campbell, H.I., Prior, K.A. and Cavanett, B.C., *Appl. Phys. Lett.*, 2004, 84(16), 3043-3045.

[24] Li, Q, Kumar, V., Li, Y., Zhang, H., Marks, T.J. and Chang, R.P.H., *Chem. Mater.*, 2005, 17, 1001-1006.

[25] Könenkamp, R., Word, R.C. and Godinez, M., *Nano Lett.*, 2005, 5(10), 2005-2008.

[26] Von Allen, M. and Blatter, A., **"Laser Beam Interaction with Materials, Physical Properties and Applications"**, 2nd edition, Springer (Berlin) (1998).

[27] Smith, R.A, **"Semiconductors"**, Cambridge University Press, 1959

This article was reviewed at Department of Semiconductors and Vacuum Electronics, University of Kharkov, UKRAINE, Department of Applied Physics, Ministry of Science and Technology, Baghdad, IRAQ, and School of Applied Sciences, University of Technology, Baghdad, IRAQ

Coming
Conferences and Symposia

INTERNATIONAL CONFERENCE ON X-RAY MICROSCOPY

21–26 July 2008
Paul Scherrer Institut, Switzerland

HFM 2008 BRAUNSCHWEIG (HIGHLY FRUSTRATED MAGNETISM)

7–12 September 2008
Branschweig, Germany

AB INITIO SIMULATION OF CRYSTALLINE SOLIDS: HISTORY AND PROSPECTS

8–9 September 2008
Torino, Italy

THE 5TH INTERNATIONAL CONFERENCE ON RADIOTHERAPY GEL DOSIMETRY (DOSGEL 2008)

September 2008
University of Heraklion, Crete, Greece

INTERNATIONAL WORKSHOP ON POSITRON STUDIES OF DEFECTS (PSD '08 PRAGUE)

September 2008
Prague, Czech Republic

THE LXIII YAMADA CONFERENCE ON PHOTO-INDUCED PHASE TRANSITION AND COOPERATIVE PHENOMENA (PIPT3)

12–15 November 2008
Osaka, Japan

Iraqi J. of Appl. Phys. , Vol. 4 , No. 1 , 2008 , 37-40

The Effect of Some Experimental Parameters on the Properties of Porous Silicon

Adawiya J. Haider

School of Applied Sciences, University of Technology, Baghdad, Iraq
adawiya_haider@yahoo.com

The influence of halogen lamp illumination intensity and HF acid concentrations on the properties of n-type porous silicon samples during the light-induced etching process were investigated. The photoluminescence (PL) spectra were recorded for porous silicon samples prepared at high illumination intensity. The peak and the shape of PL spectra are function to illumination intensities. The etching rates and porosities increases with increasing light beam intensity and go through maximum with increasing HF acid concentration.

Keywords: *Photo-chemical etching, Porous silicon, Photoluminescence*
Received 2 March 2008, Revised 20 March 2008, Accepted 25 March 2008

1. Introduction

Technological application of porous silicon (PS) as a light emitter would have a significant impact on numerous technologies such as display panels or integrated circuits with optoelectronic devices on board. Such devices require strong luminescence intensity. Porous silicon consists of a network of nanometer – sized silicon regions surrounded by void space [1]. In order to obtain PS with desired dimensions and working quantities, electrochemical etching was employed [2-4].

The formation of porous silicon in HF acid with out external biasing (Photochemical etching process) was first reported by Noguchi and Suenume by using a photon such as a high power density laser to supply the required holes in the irradiated area of the silicon wafer to initiate the etching [5]. The illumination wavelength and type of illumination (single wavelength or broad spectra) of the samples during or after the photochemical etching process is known to be an important etching parameter which can be used to modify the morphology and the photoluminescence spectra of the PS [6-8]. The purpose of this work is to prepare a PS and study the role of the halogen lamp illumination intensity and HF acid concentrations on etching rate, porosity and photoluminescence properties of (PS).

2. Experiment

Fig.1 shows a schematic diagram of experimental set-up for photochemical etching process. A commercially available mirror-like n-type (111) oriented wafer of (4.3-5.6)Ω.cm resistivity was rinsed with acetone and ethanol to remove dust and with dilute (HF) to remove the native oxide and then immersed in electronic grade HF acid. The immersed wafer was mounted on two Teflon plates and irradiated at normal incidence on the polished side in a such away that the current could pass from bottom surface to light irradiation area on the top polished surface through the electrolyte as shown in Fig. (1).

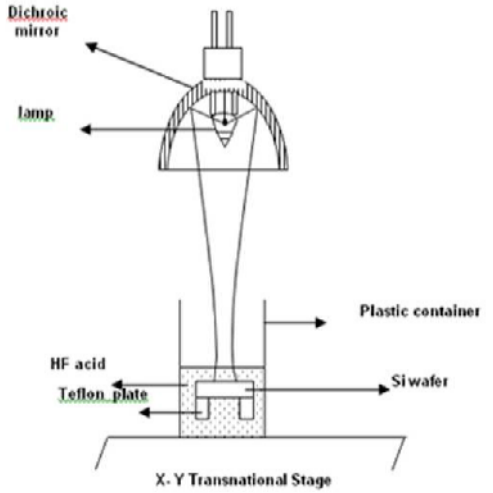

Fig. (1) Experimental set-up for Light-induced etching

In this electrode less photochemical etching process, there was no applied bias. The light beam of quartz Tungsten halogen lamp integral with dichroic ellipsoidal mirror has been focused on a silicon wafer to a circular spot (0.75cm^2) area, the distance between the halogen lamp and the wafer about (4cm). Bubbles were observed during the etching process. Wafers were etched

for 10 min at different illumination power and different HF acid concentration I_1=66.7W/cm^2, I_2=133.3W/cm^2, I_3=200W/cm^2 and I_4=333.3W/cm^2 and 10%, 20%, 30% and 40% respectively, after which they were rinsed with ethanol and dried in stream of nitrogen gas. The porous layer was formed on the mirror-like side of wafer. The value of the mean porosity over the thickness of PS layer and the thickness of PS layer were determined gravimetrically. Photoluminescence measurement was done by using He-Cd laser at a wavelength of 325nm with a low laser power density of nearly 10 mW/cm^2 in the School of Physics, Nanostructures and Optoelectronics Research Center (NOR Lab) at the University Sian in Malaysia.

3. Results and Discussion

Fig. (2) shows the relationship between the light beam intensity and the etching rate. The rates were estimated from dividing the porous layer thickness by the etching times. We can easily distinguish two regions: one at intensity up to 200W/cm^2 there is a relatively large increase in the etching rate, while the second at higher intensities, the etching rate tends to saturate (level up). The change in the slope indicates most probably a change in the reaction mechanism [9].

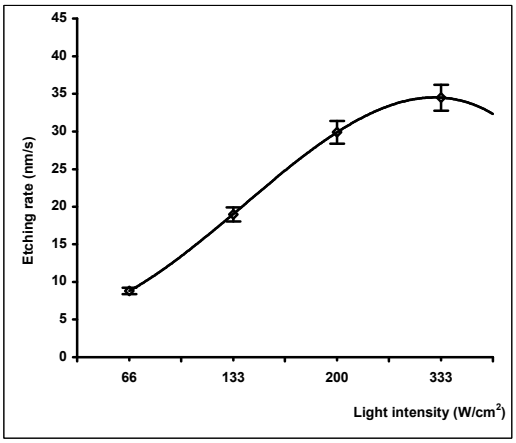

Fig. (2) the effect of light beam intensity on the etching rate of silicon nanocrystilities (nc-si), ρ=(4.3-5.6)Ω.cm

This increasing in the etching rate is due to the photon absorption of the ordinary etching light with it, larger band width from near infrared region to visible where the peak of the lamp emission around (λ=0.9μm) and this will provide a good absorption due band to band transition and also due the absorption by the impurities especially at the larger wavelengths, the absorption length which is depended on the wave length of the light is varied from (sub μm to few μm) [10], this will lead to hole formation at a different depth from the polished surface and depletion layer will form in the silicon wafer such that the polished surface is relatively positive while the back side of the wafer is negative. This created a net flow of charges from the negative to the positive side resulting in a current flow which will be completed by ions flowing in the HF solution. This net perpendicular flow of charges across the wafer will encourage the etching rate in the direction of the illumination [2, 11].

Figure (3), shows that, at a given intensity, the etching rate goes through a maximum as the HF acid concentration is increased, the maximum occurring at an HF acid mass concentration of around 30%. As the concentration of HF acid increases, there are more electron accepters in the solution, resulting in an increased rate of charge transfer between the semiconductor surface and the electrolyte [9]. Thus, band bending is larger at higher HF acid concentrations. For highly concentrated solutions of HF acid, more than 30%wt, band bending is reduced by formation of ion complexes in the solution [9, 11].

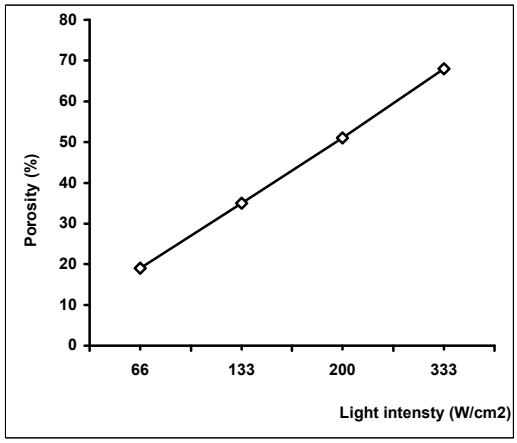

Fig. (3) The effect acid concentration on nanocrystilities (nc-si), ρ=(4.3-5.6)Ω.cm

Figure (4) shows the relationship between the light beam intensity and the porosity of the resulting porous silicon. The increasing in the illumination intensity is associated by increasing the porosity of the porous layer in approximately a linear relation this behavior is related to the silicon dissolution in the porous layer with increasing intensity [12].

Figure (5), illustrates the photoluminescence spectra of the porous silicon samples, the spectra were recorded for samples illuminated by different light beam intensity (I) 50, 100, 150, 250 and 30% HF acid concentration. The PL spectra were not obvious at low pumping intensity while are clear at high rate I_2 to I_4. These behaviors reflect the nature of the porous layer especially the morphological case.

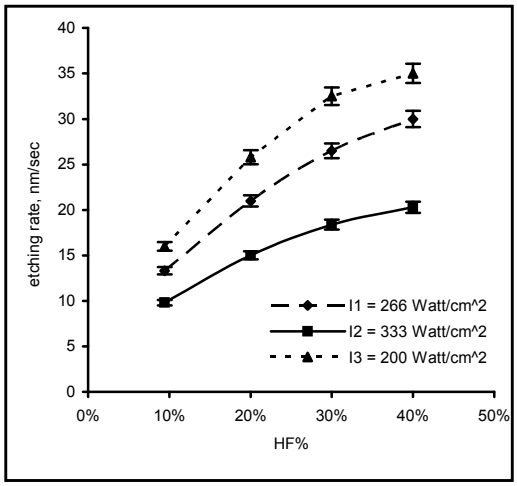

Fig. (4) The effect of light beam intensity on the porosity of PSi

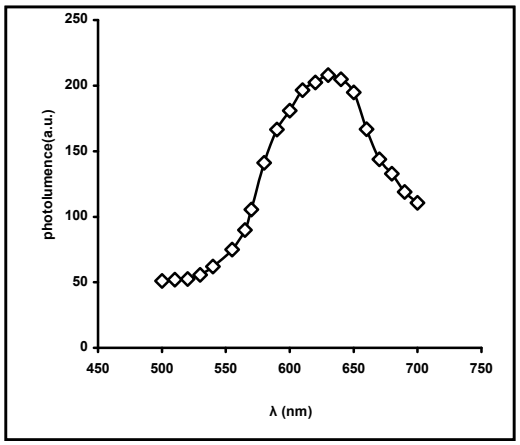

Fig. (5) PL for PS Prepared under 100W and 30% HF concentration

At low illumination intensity the porous layer may contain disconnected pits and these pits are commenced with the initiation of etching process on silicon wafers, i.e. the samples has low porosities, i.e., large size of nanocrystilities. Increasing the illumination intensity will increase the number of these pits leading to form a porous structure, [11] this structure was clear at the samples with high porosity. The increasing the porosity in porous silicon with I_2 illumination samples lead to form the nano-scale silicon [1,13-15] .In this type of silicon the photoluminescence properties at room temperature is recorded by many authors [1,8,15]. The peak of PL prepared in illumination in Fig. (6) is about (360eV) while at I_3 illumination intensity is blue shifting to (229eV). This is attributed to size of silicon nanocrystilities, according to quantum confinement (QC) effects [15], and

$$E_{g_{new}} = E_{g_{bulk}} + \frac{88.34}{L^{1.37}} \qquad (1)$$

the average nano-size is (2.006eV) for Fig. (6) and (2eV) for Fig. (5).

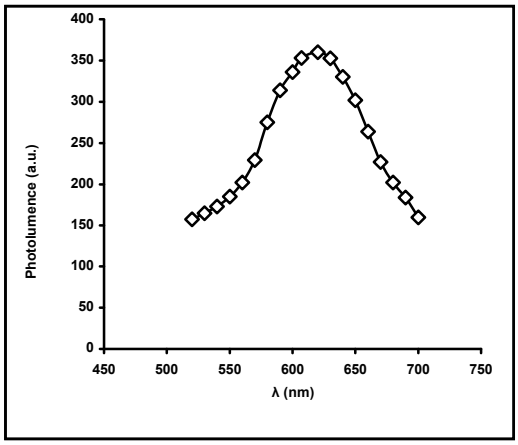

Fig. (6) PL for PS Prepared under 150W and 30% HF concentration

As shown in Fig. (7), the PL properties for samples shows in addition to the blue shifting, presses a new peak at (2.1eV) in addition to the (3.03eV) peak. This behavior refers to form a double porous layer one at low nano-size a bout (410nm) and another at (580nm). This may due to the excessive etching of the first layer leading to form small nano-size. This layer may presses at the surface of PS layer [12,15].

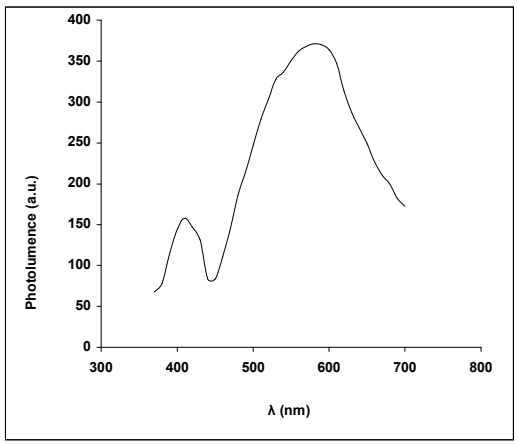

Fig. (7) PL for PS Prepared under 250W and 30% HF concentration

4. Conclusion

The variation of the HF acid concentration and illumination intensity during porous silicon formation causes dramatic changes in the porous silicon properties. We found that the etching rates and the porosity of the porous layer increases with illumination intensity of the halogen lamp and go through maximum with increasing HF acid concentration. The main reason for increasing the etching rate and hence the porosity might be related to electron hole generation by the light radiation and transport holes to the surface .the PL spectra is observed just from the porous silicon samples at high illumination intensities only. The PL spectra this

may relate to the fact that at high porosities the amount is a function to the illumination intensity with a blue shifting.

Acknowledgement

The author is grateful to Dr. N.M. Alrawi for the measurement facilities, as well as to Prof. A.M.I. Ahmed and A.M. Alwan for many useful discussions.

References

[1] L.T. Canham , *Appl. Phys. Lett.*, 57 (1990) 1046.
[2] M.I.J. Beale et al., *J. Cryst. Growth*, 73 (1985) 622.
[3] H. Gerischer and M. Lübke, Ber. Bunsen-Ges, *J. Phys. Chem.*, 91 (1987) 394.
[4] V. Lehmann, *J. Electrochem. Soc.*, 140 (1993) 2836.
[5] N. Nouguchi and I. Suemune, *Appl. Phys. Lett*., 62 (1993) 1429.
[6] V. Lehmann, H. Cerva and U. Gosele, *Mater. Res. Soc. Symp. Proc.*, 256 (1992).
[7] M. Thonissen et al., *Thin Solid Films*, 276 (1996) 21.
[8] H. Mavi et al., *J. Non-Cryst. Solids*, 162 (2001) 286.
[9] P. Lim, J. Brock and I. Trachtenberg, *Appl. Phys. Lett.*, 60(4) (1992) 27.
[10] D.E. Aspen and A.A. Studna, *Phys. Rev. B.*, 27 (1983) 985.
[11] L. Koker and K.W. Kolasinki, *J. Phys. Chem.*, 2 (2000) 277.
[12] B.G. Rasheed, "Spectroscopy of Porous Silicon Prepared By Laser-Induced Etching", PhD thesis, Indian Institute of Technology, Delhi, India (2003).
[13] C. Peng and K. Hirschman, *J. Appl. Phys.*, 80 (1996) 295.
[14] N. Lalic, "Light Emitting Devices Based on Silicon Nanostructures", PhD thesis, KTH, Royal Institute of Technology, Stockholm (2000).
[15] L. Canham, **"Properties of Porous Silicon"**, INSPEC (U.K.) 2004.

This article was reviewed at School of Electrical and Electronic Engineering, Nanyang Technological University, SINGAPORE, Department of Applied Physics, Ministry of Science and Technology, IRAQ, and School of Applied Sciences, University of Technology, Baghdad, IRAQ

Coming

Conferences and Symposia Sponsored by SPIE

19th International Conference on Optical Fibre Sensors
14 - 18 April 2008
Location: Perth, WA, Australia

Scanning 2008
15 - 17 April 2008
Location: Gaithersburg, Maryland, USA

Photomask Japan 2008
16 - 18 April 2008
Location: Yokohama, Japan

SPIE/OSA/IEEE-LEOS International Symposium on Optical Memory and Optical Data Storage
13 - 17 July 2008
Location: Waikoloa, Hawaii, USA
Exhibition: 14 - 17 July 2008

SPIE Optics + Photonics
10 - 14 August 2008
Location: San Diego, California, USA
Exhibition: 12 - 14 August 2008

NanoScience + Engineering, part of Optics+Photonics 2008
10 - 14 August 2008
Location: San Diego, California, USA

Solar Energy + Applications, part of Optics+Photonics 2008
10 - 14 August 2008
Location: San Diego, California, USA

Photonic Devices + Applications, part of Optics+Photonics 2008
10 - 14 August 2008
Location: San Diego, California, USA

Optical Engineering + Applications, part of Optics+Photonics 2008
10 - 14 August 2008
Location: San Diego, California, USA

SPIE Europe Optical Systems Design
2 - 5 September 2008
Location: Glasgow, Scotland, UK
Exhibition: 3 - 4 September 2008

SPIE Europe Security + Defence
15 - 18 September 2008
Location: Cardiff, Wales, UK
Exhibition: 16 - 17 September 2008

SPIE Europe Remote Sensing
15 - 18 September 2008
Location: Cardiff, Wales, UK

Boulder Damage Symposium XL Annual Symposium on Optical Materials for High Power Lasers
22 - 24 September 2008
Location: Boulder, CO, USA

SPIE Photomask Technology 28th Annual Symposium
6 - 10 October 2008
Location: Monterey, California, USA
Exhibition: 7 - 8 October 2008

SPIE APOC 2008 Asia-Pacific Optical Communications
26 - 30 October 2008
Location: Hangzhou, China

SPIE Lithography Asia - Taiwan
4 - 6 November 2008
Location: Taipei, Taiwan

International Symposium on Optomechatronic Technologies
17 - 21 November 2008
Location: San Diego , California, USA

SPIE Asia-Pacific Remote Sensing
17 - 21 November 2008
Location: Noumea, New Caledonia

IRAQI JOURNAL OF APPLIED PHYSICS

" INSTRUCTIONS TO AUTHORS "

A new Iraqi specialized quarterly periodical dedicated to publishing original papers and letters in:

Applied & Nonlinear Optics	Electronic Materials & Devices	Quantum Physics & Spectroscopy
Applied Mechanics & Thermodynamics	Laser Physics & Applications	Semiconductors & Optoelectronics
Digital & Optical Communications	Plasma Physics & Applications	Solid State Physics & Applications

CONTRIBUTIONS

Contributions to be published in this journal should be original research works, i.e., those not already published or submitted for publication elsewhere, individual papers or letters to editor.

SUBMISSION OF MANUSCRIPTS

Manuscripts should be submitted to the editor at the mailing address:

Iraqi Journal of Applied Physics
Managing Editor
P. O. Box 55259, Baghdad 12001, IRAQ
irq_appl_phys@yahoo.com

Iraqi Journal of Applied Physics
Editor-In-Chief
P. O. Box 55159, Baghdad 12001, IRAQ
editor_ijap@yahoo.co.uk

MANUSCRIPTS

Two copies with soft copy on a compact disc (CD) should be submitted to Editor in the following configuration:

- Double-spaced one-side A4 size with 2.5 cm margins of all sides
- 12pt Times New Roman font
- Letters should not exceed 5 pages, papers no more 20 pages and reviews are up to author.
- Manuscripts presented in English only are accepted.
- Authors confirm affiliations, addresses and emails. Email is necessary for correspondences.
- English abstract not exceed 150 words
- 4 keywords (at least) should be maintained on (PACS preferred)
- Author(s) should express all quantities in SI units
- Equations should be written in equation form (italic and symbolic)
- Figures and Tables should be separated from text
- Figures and diagrams can be submitted in colors for assessment and they will be returned to authors after provide printable copies
- Charts should be indicated by the software used for
- Only original or high-resolution scanner photos are accepted
- References are written in titles, full-name authors, names of publications, years, volumes, issues and pages (from-to)

PROOFS

Authors will receive proofs of papers and are requested to return one corrected hard copy with a WORD copy on a compact disc (CD). New materials inserted in the original text without Editor permission may cause rejection of paper.

COPYRIGHT FORM

Author(s) will be asked to transfer copyrights of the article to the Journal soon after acceptance of it. This will ensure the widest possible dissemination of information.

OFFPRINTS

Authors will receive offprints free of charge and any additional offprints can be ordered.

SUBSCRIPTION AND ORDERS

Annual fees (4 issues per year) of subscription are:

50 000 Iraqi dinars for individuals and establishments inside Iraq.
50 US$ for individuals and establishments abroad.

I.S.A.R.E.S.T. members have 25% discount of fees. Orders of issues can be submitted by contacting the editor-in-chief or editorial secretary to maintain the address of issue delivery and payment way.

COPYRIGHY RELEASE

Iraqi Journal of Applied Physics (IJAP)

We, the undersigned, the author/authors of the article titled

……

……

……

……

that is presented to the Iraqi Journal of Applied Physics (IJAP) for publication, declare that we have neither taken part or full text from any published work by others, nor presented or published it elsewhere in any other journal. We also declare transferring copyrights and conduct of this article to the Iraqi Journal of Applied Physics (IJAP) after accepting it for publication.

The authors will keep the following rights:

1. Possession of the article such as patent rights.
2. Free of charge use of the article or part of it in any future work by the authors such as books and lecture notes without referring to the IJAP.
3. Republishing the article for any personal purposes of the authors after taking journal permission.

To be signed by all authors:

Signature:……..date: ……..

Printed name: ……..

Signature:……..date: ……..

Printed name: ……..

Signature:……..date: ……..

Printed name: ……..

Correspondence address:

……

……

Telephone:……Fax:……..email: ……

Note: Please complete and sign this form and mail it to the below address with your manuscript

The Iraqi Journal of Applied Physics,
P. O. Box 55259, Baghdad 12001, IRAQ
Email: *irq_appl_phys@yahoo.com* or *editor_ijap@yahoo.co.uk*
Mobile: +964-7901274190

IRAQI JOURNAL OF APPLIED PHYSICS

CONTENTS